Diode Equation for Sandwich-Type Thin-Film Photovoltaic Devices Limited by Bimolecular Recombination

Oskar J. Sandberg[1,*] and Ardalan Armin[2]

[1] *Physics, Faculty of Science and Engineering, Åbo Akademi University, Henrikinkatu 2, 20500 Turku, Finland*
[2] *Sustainable Advanced Materials (Sêr-SAM), Centre for Integrative Semiconductor Materials (CISM), Department of Physics, Swansea University Bay Campus, Swansea SA1 8EN, United Kingdom*

(Received 18 July 2023; revised 4 April 2024; accepted 31 May 2024; published 21 June 2024)

Analytical diode models that relate the current to key material parameters are invaluable for understanding the device physics in photovoltaic (PV) devices. However, a diode model that accurately describes the current in thin-film PVs based on low-mobility semiconductors (including organic solar cells) limited by bimolecular recombination has been lacking. Previous models neglect effects of injected charge carriers, which are the predominant source for bimolecular recombination in thin-film PV systems with Ohmic contacts. In this work, we derive a unified diode equation for thin-film PVs based on undoped semiconductors limited by bimolecular recombination. Based on a regional approximation approach, we derive an analytical model for the current accounting for the interplay between charge-carrier extraction, injection, and bimolecular recombination. The analytical model is validated by numerical simulations and tested experimentally on organic solar cells. Our findings provide key insights into the mechanisms driving and limiting charge collection, and ultimately the power-conversion efficiency, in low-mobility PV devices. The presented framework is material agnostic and generally applicable to sandwich-type thin-film PV devices, including photodiodes and indoor light-harvesting cells.

DOI: 10.1103/PRXEnergy.3.023008

I. INTRODUCTION

Sandwich-type thin-film photovoltaics based on undoped semiconductors play an important role in emerging and sustainable solar cell technologies [1,2]. To advance the performance of these technologies it is vital to understand processes limiting important device metrics such as the current-voltage (J-V) characteristics. The J-V characteristics of photovoltaic devices are commonly analyzed in terms of the ideal-diode equation, which assumes a constant photocurrent [2,3]. However, in thin-film devices limited by low charge-carrier mobilities ($\mu < 1$ cm^2/Vs), the charge collection is generally assisted by the internal electric field [4,5], resulting in an electric-field-dependent photocurrent and, ultimately, a deviation from the ideal-diode equation [6,7]. Notable examples include organic semiconductor-based photovoltaics (OPVs) and a-Si solar cells. OPVs have recently displayed a rapid increase in solar cell performance [8], while also showing promise for use in low-light-intensity applications such as indoor light harvesting [9].

Ideally, these devices constitute an intrinsic active layer sandwiched between two charge-carrier selective contact layers, forming a p^+-i-n^+-like structure. To analytically describe the current in devices with low mobilities, the competition between the charge extraction and recombination of photogenerated charge carriers needs to be accounted for [6,10,11]. In general, the recombination of free electrons and holes in low-mobility materials occurs either by bimolecular recombination or by Shockley-Read-Hall (SRH) recombination via traplike states within the energy gap [5,12]. Crandall derived an analytical model of the photocurrent for the case when SRH recombination via deep traps is the dominant recombination channel [13]. This treatment was later extended to fully account for effects of injected carriers by Taretto [14]. While trap-assisted recombination can in principle be mitigated by minimizing the density of impurities and energetic disorder, bimolecular recombination is unavoidable, setting the ultimate limit for recombination in any photovoltaic device. However, analytical models for the current in the case of bimolecular recombination have thus far been derived only for situations that simplify or omit effects of injected carriers from the contacts [6,15–17].

*Corresponding author: oskar.sandberg@abo.fi

Injected carriers are inevitably present in any thin-film device with Ohmic contacts [18,19]. These carriers are characterized by highly nonuniform, voltage-dependent charge-carrier profiles and have been found to cause energy level bending, reducing the magnitude of the built-in electric field inside the active layer [14,20]. In addition, recombination between injected carriers and photogenerated carriers has been shown to be a dominant bimolecular recombination channel in OPVs causing first-order photocurrent losses, manifesting as nonideal fill factors (FFs) regardless of light-intensity regime [21,22]. To our knowledge, an explicit diode equation fully describing the interplay between charge-carrier extraction, injection, and bimolecular recombination in low-mobility thin-film devices has yet to be established.

In this work, we derive a diode equation describing the *J-V* characteristics of thin-film photovoltaic devices limited by bimolecular recombination. Using a regional approximation approach, expressions for the current are obtained that, for the first time, fully account for the interplay between charge-carrier extraction, injection, and bimolecular recombination in sandwich-type thin-film devices. The derived approximations are validated by numerical drift-diffusion simulations and applied to experimental OPV results. The obtained findings provide valuable insight into the mechanisms driving and limiting charge collection in low-mobility systems. Additionally, the presented analytical framework provides a figure-of-merit that parametrizes *J-V* curves more accurately than previous models, useful for fitting experimental data to extract key material properties. Such parametrization may also find applications in labeling input *J-V* data for training machines used for device optimization [23,24]. The developed theoretical framework is material agnostic and generally applicable to thin-film photovoltaic devices based on undoped semiconductors with Ohmic contacts.

II. THEORETCIAL BACKGROUND

For a given applied voltage V across the active layer, the total current density J of a thin-film diode device is determined by the flow of electrons and holes within the device. Under steady-state conditions, $J = J_n(x) + J_p(x)$, where $J_n(x)$ and $J_p(x)$ are the electron and hole current density, respectively, at any position x inside the active layer. The electron and hole current densities are related to the photogeneration rate G and recombination rate R of charge carriers within the active layer via the carrier continuity equations,

$$-\frac{1}{q}\frac{\partial J_n}{\partial x} = \frac{1}{q}\frac{\partial J_p}{\partial x} = G(x) - R(x), \tag{1}$$

where q is the elementary charge and $0 < x < d$, with d being the active layer thickness, assuming an active layer sandwiched between an anode ($x = 0$) and a cathode ($x = d$) contact. Further, assuming an effective medium description, $J_n(x)$ and $J_p(x)$ depend on their respective electron and hole densities $n(x)$ and $p(x)$ through the drift-diffusion relations as follows [3,25]:

$$J_n(x) = \mu_n n(x)\frac{\partial E_{Fn}}{\partial x} = \mu_n\left[qn(x)F(x) + kT\frac{\partial n}{\partial x}\right], \tag{2}$$

$$J_p(x) = \mu_p p(x)\frac{\partial E_{Fp}}{\partial x} = \mu_p\left[qp(x)F(x) - kT\frac{\partial p}{\partial x}\right]. \tag{3}$$

Here, μ_n (μ_p) is the electron (hole) mobility, E_{Fn} (E_{Fp}) the quasi-Fermi level of electrons (holes), F the electric field, k the Boltzmann constant, and T the absolute temperature. The classical Einstein relation for the electron (hole) diffusion constant, $D_{n(p)} = \mu_{n(p)}kT/q$, has been assumed in the second equality of Eqs. (2) and (3).

The electric field inside the active layer depends on the densities of free charge carriers through the Poisson equation. In the case of an undoped and trap-free active layer, the Poisson equation is given by

$$\frac{\partial F}{\partial x} = \frac{q}{\varepsilon\varepsilon_0}[p(x) - n(x)], \tag{4}$$

with ε being the relative permittivity of the active layer and ε_0 the vacuum permittivity. The electric field is related to the electrical potential $\phi(x)$ inside the active layer via $F(x) = -\partial\phi/\partial x$; in this work we define $\phi(x) = -\int_0^x F(x')dx'$ with $\phi(0) = 0$ as the reference potential level. Note that $\phi(x)$ is proportional to the effective conduction level $E_c(x)$ in the acceptor and valence level $E_v(x)$ in the donor as $q[\phi(x) - \phi(0)] = E_v(0) - E_v(x)$, while $E_c(x) = E_v(x) + E_g$ with E_g being the effective transport level gap.

In this work, the dominant recombination channel for free charge carriers in the bulk is assumed to be bimolecular recombination, corresponding to an active layer material with low defect density and small energetic disorder. Accordingly, the net bulk recombination rate is of the form

$$R(x) = \beta n(x)p(x) - \beta n_i^2, \tag{5}$$

where β is the bimolecular recombination rate coefficient. The effect of trap-assisted recombination and other recombination channels is discussed in Sec. III F below. In Eq. (5), the term βn_i^2 defines the thermal (dark) generation rate of free charge carriers within the active layer, where $n_i^2 = N_c N_v \exp(-E_g/kT)$ with N_c (N_v) being the effective density of the conduction (valence) level.

It should be noted that the generation and bimolecular recombination of free charge carriers in organic semiconductors generally take place via bound excitonic states and charge-transfer (CT) states [8,26–30]. As such, the corresponding G and β are expected to depend on

the exciton and CT state kinetics [31]. In this picture, $\beta = (1 - P_{CT})\beta_0$, which involves the encounter of free electrons and holes (described by rate constant β_0) [32] and the formation and subsequent decay of the bound states to the ground state (with a probability of $1 - P_{CT}$) [31]. The latter process is believed to be the leading source of nonradiative recombination in OPV solar cells [33–35]. β is commonly compared to the Langevin recombination constant $\beta_L = q[\mu_n + \mu_p]/(\varepsilon\varepsilon_0)$ [36], considered to be the upper limit for β in low-mobility systems.

Based on Eqs. (1) and (5), the total current density can be expressed as

$$J = -J_{gen} + q\beta \int_0^d [n(x)p(x) - n_i^2]dx + J_n(0) + J_p(d), \tag{6}$$

where $J_{gen} \equiv q\int_0^d G(x)dx$ is the saturated photogeneration current density. In this work, we consider contacts that are ideally selective for the extraction of majority carriers (electrons at cathode, holes at anode). In other words, majority carriers are assumed to remain at thermal equilibrium at the contacts, such that $p(0) = p_{an}$ and $n(d) = n_{cat}$, while $J_n(0) = J_p(d) = 0$ (no surface recombination of minority carriers). Here, p_{an} (n_{cat}) is the corresponding thermal equilibrium density for holes (electrons) at the anode (cathode). Finally, V is related to $F(x)$ via

$$V - V_{BI,0} = \int_0^d F(x)dx, \tag{7}$$

where $qV_{BI,0} = kT\ln(p_{an}n_{cat}/n_i^2)$ corresponds to the work function difference between the anode and cathode contact.

To evaluate J for a given V, the set of coupled differential equations Eqs. (1)–(5) needs to be solved for $\phi(x)$, $n(x)$, and $p(x)$. In the next section, we present an analytical framework for J based on approximative solutions of $\phi(x)$, $n(x)$, and $p(x)$. To validate the obtained approximate expressions, we compare them with the results of numerical simulations representing the "exact" solutions. For this purpose, we use a previously established numerical device model (see Ref. [37]), based on the Scharfetter-Gummel discretization scheme and Gummel's iteration method [38–40]. In the simulations, we consider an active layer having $d = 100$ nm, $N_v = N_c = 10^{21}$ cm^{-3}, and an energy level gap of $E_g = 1.42$ eV. Further, we assume a uniform photogeneration rate ($G(x) = G$) that scales linearly with light intensity and takes a value of 6.24×10^{21} cm^{-3} s^{-1} under 1-sun conditions. Unless otherwise stated, balanced mobilities ($\mu = \mu_n = \mu_p$) are assumed in the simulations. Finally, we assume that the contacts are Ohmic, corresponding to injecting contacts at which the carrier density is high enough (negligible resistance) to not limit the majority-carrier current. To ensure this condition, we assume $p_{an} = N_v$ and $n_{cat} = N_c$.

III. RESULTS AND DISCUSSION

In Fig. 1 the effect of the interplay between charge collection and bimolecular recombination on the *J-V* characteristics is demonstrated. A photovoltaic device with $\mu = 10^{-4}$ cm^2/Vs is simulated and compared with the idealized case with perfect charge collection ($\mu \to \infty$), assuming a fixed $\beta = 10^{-10}$ cm^3/s. Figures 1(a) and 1(b) show the normalized currents J/J_{gen} under 1-sun (solar cell) and 0.001-sun (relevant for indoor PVs) illumination conditions, respectively. Independent of the light intensity, decreasing μ generally reduces both the short-circuit current density (J_{SC}) and the FF. This suggests that, even at low light intensities, there can be a substantial charge collection loss caused by bimolecular recombination in the case of low mobilities. Conversely, in the limit of high mobilities, both J_{SC} and FF saturate to their maximum values (set by the prevailing intensity) as $J_{SC} \to J_{gen}$. Note that the open-circuit voltage (V_{OC}) is independent of μ in this case (since β is fixed) and depends only on the light intensity. For an analytical model of the *J-V* characteristics to be accurate, it is imperative that it reproduces the mobility- and intensity-dependent behaviors in Fig. 1. In the following, approximations relating the current and bimolecular recombination in sandwich-type thin-film PV devices with Ohmic contacts are derived.

A. Analytical approach

To obtain approximate solutions for the charge-carrier transport equations, we use the following ansatz for the electron and hole density:

$$n(x) = n_0(x) + \Delta n(x), \tag{8}$$

$$p(x) = p_0(x) + \Delta p(x). \tag{9}$$

Here, $n_0(x)$ and $p_0(x)$ are defined as the respective ideal carrier densities expected in case of flat quasi-Fermi levels ($\partial E_{Fn}/\partial x = \partial E_{Fp}/\partial x = 0$) separated by qV. In accordance with Eqs. (2) and (3), we have, by definition, that

$$qn_0(x)F(x) = -kT\frac{\partial n_0(x)}{\partial x}, \tag{10}$$

$$qp_0(x)F(x) = kT\frac{\partial p_0(x)}{\partial x}, \tag{11}$$

for every x inside the active layer. Noting that $J = J_n(x) = J_p(x) = 0$ at open circuit, it directly follows that $n(x) = n_0(x)$ and $p(x) = p_0(x)$ at $V = V_{OC}$. In other words, $n_0(x)$ and $p_0(x)$ at any given applied voltage V in the dark are identical to the respective $n(x)$ and $p(x)$ obtained at open circuit under a light intensity that results in a V_{OC} equal to V.

Conversely, $\Delta n(x)$ and $\Delta p(x)$ represent the corresponding deviations of $n(x)$ and $p(x)$ from their ideal carrier

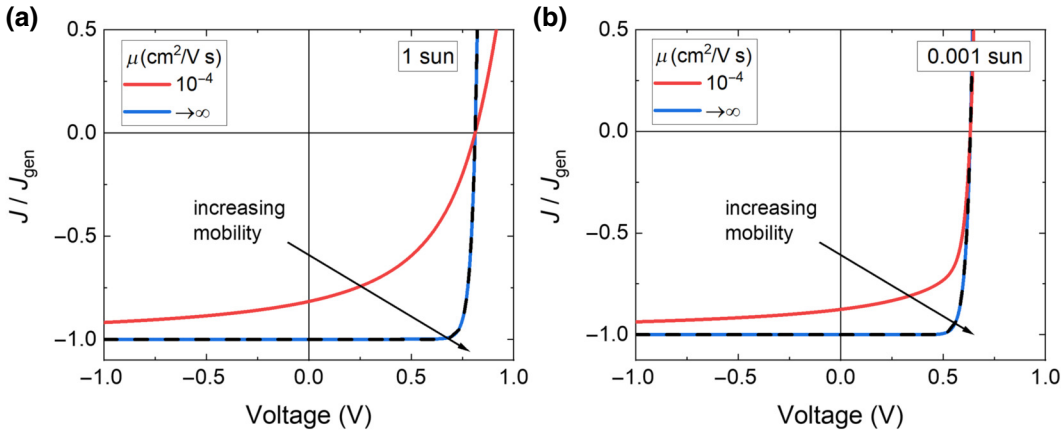

FIG. 1. Simulated J-V characteristics of a sandwich-type thin-film PV device under (a) 1-sun and (b) 0.001-sun illumination conditions demonstrating the effect of finite mobilities on the current density. The case of balanced mobilities with $\mu = 10^{-4}$ cm^2/Vs (red line) is shown and compared to the idealized case of $\mu \to \infty$ (blue line). A fixed bimolecular recombination coefficient $\beta = 10^{-10}$ cm^3/s is assumed for both cases. The predictions based on the ideal-diode equation Eq. (17) are indicated by black dashed lines.

densities. $\Delta n(x)$ and $\Delta p(x)$ are determined by the charge-carrier transport properties inside the device. Making use of Eqs. (10) and (11), in conjunction with Eqs. (2) and (3), in Eq. (1) the electron and hole continuity equations can be expressed as

$$\mu_n F\frac{\partial \Delta n}{\partial x} + \mu_n \Delta n\frac{\partial F}{\partial x} + \mu_n \frac{kT}{q}\frac{\partial^2 \Delta n}{\partial x^2} = -G + \beta[p_0 n_0 - n_i^2 + p_0\Delta n + n_0\Delta p + \Delta n\Delta p], \tag{12}$$

$$\mu_p F\frac{\partial \Delta p}{\partial x} + \mu_p \Delta p\frac{\partial F}{\partial x} - \mu_p \frac{kT}{q}\frac{\partial^2 \Delta p}{\partial x^2} = G - \beta[p_0 n_0 - n_i^2 + p_0\Delta n + n_0\Delta p + \Delta n\Delta p]. \tag{13}$$

While general analytically tractable solutions to Eqs. (12) and (13) cannot be found, approximate expressions can be obtained depending on the dominant recombination terms. Note that Δn and Δp should primarily be considered mathematical tools that may take positive or negative values. In regions where $\Delta n \gg n_0$ ($\Delta p \gg p_0$) applies, however, Δn (Δp) may be identified as the excess density of photogenerated electrons (holes).

1. Ideal charge collection

We first consider the idealized zeroth-order case, when $n(x) \to n_0(x)$ and $p(x) \to p_0(x)$. Excluding open-circuit conditions, this corresponds to the limit of infinite mobilities (or ideal conductivities). This follows from the fact that for $J_n(x)$ and $J_p(x)$ to remain finite as μ_n and μ_p approach infinity, we must generally have

$$\frac{\partial E_{Fn}}{\partial x} = \frac{\partial E_{Fp}}{\partial x} \to 0.$$

Figures 2(a) and 2(b) show the carrier densities inside the active layer (under the 1-sun illumination condition) for different mobilities at $V = 0$ and $V = 0.5$ V, respectively. The corresponding energy level diagrams are depicted in Figs. 2(c) and 2(d). As expected, E_{Fn} and E_{Fp} in the limit of high mobilities are flat throughout the active layer and separated by qV. In other words, the free carriers are in electrochemical equilibrium with their collecting electrodes.

As $n(x) \to n_0(x)$ and $p(x) \to p_0(x)$, the recombination rate is dominated by the $\beta p_0(x) n_0(x)$ term in Eqs. (12) and (13) (i.e., the zeroth-order term with respect to photogenerated carriers). This term can be directly evaluated noting that $n_0(x)$ and $p_0(x)$, as per Eqs. (10) and (11), can be equivalently expressed as

$$n_0(x) = n_{\text{cat}}\exp\left(\frac{q[V - V_{\text{BI},0} + \phi(x)]}{kT}\right), \tag{14}$$

$$p_0(x) = p_{\text{an}}\exp\left(-\frac{q\phi(x)}{kT}\right). \tag{15}$$

As a result, in this limit $n_0(x)p_0(x)$, and thus the bimolecular recombination rate, is independent of the position inside the active layer. Making use of the definition of $V_{\text{BI},0}$, the generalized mass action law is further obtained as

$$n_0(x)p_0(x) = n_i^2\exp\left(\frac{qV}{kT}\right). \tag{16}$$

Hence, for selective contacts ($J_n(0) = J_p(d) = 0$), the total current density [Eq. (6)] in the limit of ideal charge collection ($\mu_{n,p} \to \infty$) is given by

$$J_{\text{ideal}}(V) = -J_{\text{gen}} + J_0\left[\exp\left(\frac{qV}{kT}\right) - 1\right], \tag{17}$$

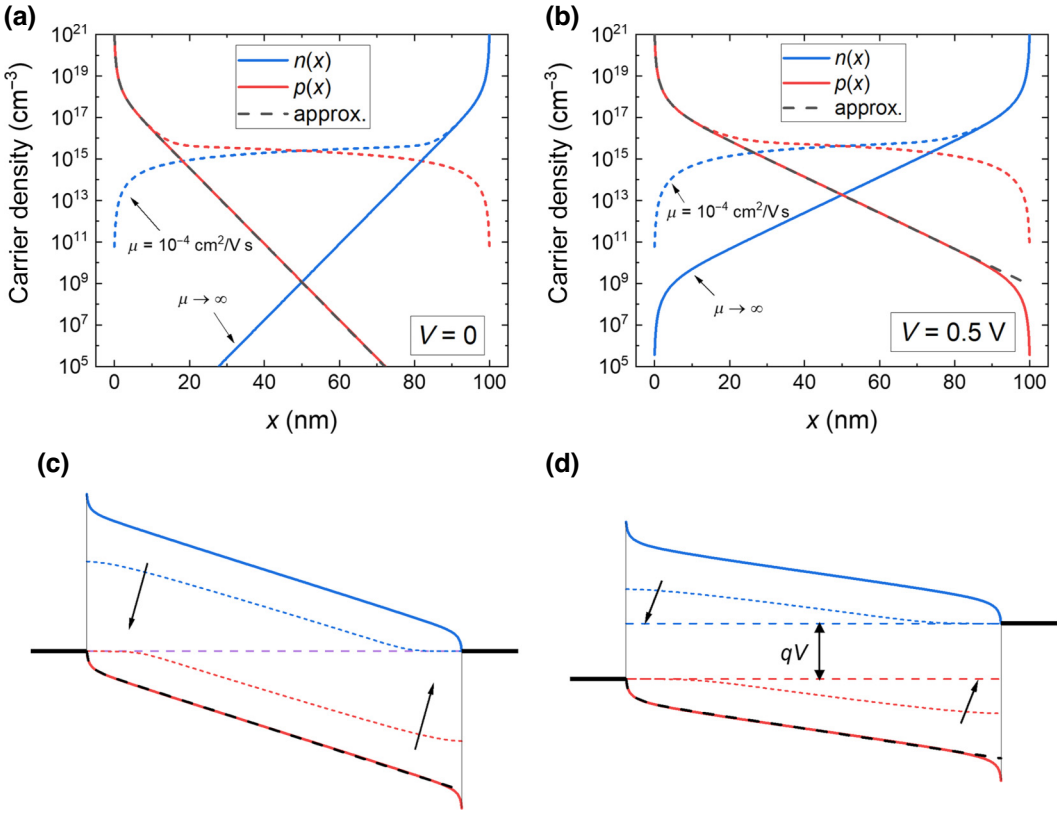

FIG. 2. Simulated carrier density profiles of the thin-film PV device from Fig. 1 at 1 sun for (a) $V = 0$ and (b) $V = 0.5$ V. The solid and dotted lines indicate the case of $\mu \to \infty$ and $\mu = 10^{-4}$ cm^2/V s, respectively. In (c),(d), the corresponding energy level diagrams for $V = 0$ and $V = 0.5$ V are shown, respectively. The conduction and valence levels are indicated by blue and red solid lines, respectively, while the electron and hole quasi-Fermi levels are indicated by blue and red dashed lines. For comparison, the analytical approximations based on Eqs. (15) and (19) are depicted by the black dashed lines.

where $J_0 = q\beta n_i^2 d$ is the dark saturation current density induced by thermal generation of charge carriers in the active layer. As expected, in the high-mobility limit, $J(V)$ is of an identical form to the ideal-diode equation. Indeed, Eq. (17) (indicated by the dashed lines) precisely reproduces the simulated J-V curves when $\mu \to \infty$ in Fig. 1.

2. Regional approximation

Based on Eqs. (14) and (15), expressions for the ideal carrier densities can be derived by making use of a regional approximation. In the ideal limit, the densities of electrons and holes dominate at cathode and anode contacts, respectively, while they decrease exponentially away from the contact [see Figs. 2(a) and 2(b)]. Subsequently, the active layer can be divided into a hole-dominated ($0 < x < x^*$) and an electron-dominated region ($x^* < x < d$), where x^* is the width of the hole-dominated region. Assuming that $p_0 \gg n_0$ in the hole-dominated region, analytical approximations for $p_0(x)$ can be obtained [19,41]. For $x < x^*$, Eq. (4) then simplifies as

$$\frac{\partial F(x)}{\partial x} = -\frac{\partial^2 \phi(x)}{\partial x^2} \approx \frac{q p_0(x)}{\varepsilon \varepsilon_0}. \tag{18}$$

Substituting Eq. (15) into Eq. (18) and solving for $\phi(x)$ yields

$$\phi(x) = \frac{2kT}{q} \ln\left(\frac{2kT}{qF_0\lambda_{an}} \sinh\left[\frac{qF_0 x}{2kT} + \sinh^{-1}\left(\frac{qF_0\lambda_{an}}{2kT}\right)\right]\right), \tag{19}$$

for $F_0 \gg 2kT/qd$, where $\lambda_{an} = \sqrt{2\varepsilon\varepsilon_0 kT/[q^2 p_{an}]}$ represents the Debye screening length for holes at the anode contact and F_0 is an integration constant of the electric field. Thus, the electric field in this region is obtained as

$$F(x) = -F_0 \coth\left[\frac{qF_0 x}{2kT} + \sinh^{-1}\left(\frac{qF_0\lambda_{an}}{2kT}\right)\right]. \tag{20}$$

Note that sufficiently far from the contact, $F \to -F_0$ in Eq. (20). Concomitantly, F_0 represents the magnitude of the electric field deep inside the active layer. A completely analogous treatment applies for $x > x^*$ (assuming $n_0 \gg p_0$) [42]. Demanding that $F(x)$ is continuous at $x = x^*$, it can be shown that $x^* \approx d/2$ for Ohmic contacts, corresponding to $\lambda_{an}, \lambda_{cat} \ll d$, where λ_{cat} is the corresponding Debye screening length for electrons at the cathode

contact. Finally, an expression for F_0 can be obtained after matching $\phi(x)$ at $x = x^*$ and applying the boundary condition Eq. (7).

In general, F_0 depends on the contact properties (represented by λ_{an}, λ_{cat}, and $V_{BI,0}$) and the applied voltage through a transcendental dependence. In the case of Ohmic contacts ($\lambda_{an}, \lambda_{cat} \ll d$), however, F_0 may be approximated as follows [42]:

$$F_0 \approx \frac{1}{d}\left[V_{BI} - V\left(1 + \frac{\ln|2|}{(qV_{BI}/8kT) - 1}\right)\right], \tag{21}$$

for $V_{BI} - V > 8\ln(2)kT/q$. Herein, V_{BI} is the effective built-in voltage inside the active layer at $V = 0$, determined via

$$V_{BI} = V_{BI,0} - \frac{2kT}{q}\ln\left(\frac{q^2d^2\sqrt{p_{an}n_{cat}}}{2\varepsilon\varepsilon_0 kT}\right) + \frac{4kT}{q}\ln\left(\frac{qV_{BI}}{kT}\right). \tag{22}$$

Note that the effective built-in voltage inside the active layer is reduced relative to the electrode work function difference $V_{BI,0}$ because of energy level bending near the contacts, as seen in Figs. 2(c) and 2(d). This energy level bending also depends on the applied voltage, which is accounted for by the final term within the round brackets on the right-hand side of Eq. (21).

In Fig. 2, $p_0(x)$ predicted by Eq. (15) (dashed lines), with $\phi(x)$ given by Eq. (19), are compared with the simulated $p(x)$ (solid lines). Indeed, Eq. (15) reproduces the simulated $p(x)$ in the limit $\mu_p \to \infty$. Inside the active layer, Eq. (19) predicts $\phi(x)$ to be linearly dependent on x, translating into exponentially varying carrier densities in this limit. Near the contacts, however, the accumulation of majority carriers induces significant energy level bending resulting in nonexponential behavior within these regions. It should be noted that, although initially derived for $x < x^*$, the approximation based on Eq. (19) generally applies beyond this region; in fact, except for the electron-accumulation region near the cathode contact, Eq. (19) remains a good approximation for $\phi(x)$ throughout the entire active layer.

In the case of finite mobilities, Eq. (15) is also seen to accurately describe $p(x)$ within the anode contact region; this is a consequence of the high hole density resulting in a virtually flat E_{Fp} [cf. Eq. (3)], and thus $p(x) = p_0(x)$ within this region. Subsequently, the majority carrier densities within the contact regions are independent of charge-transport properties, consistent with the defining characteristic of Ohmic contacts. Finally, the $E_v(x)$ predicted based on Eq. (19) (dashed line) are compared with the simulated $E_v(x)$ (solid lines) in Figs. 2(c) and 2(d); an excellent agreement is obtained. It should be noted that the simulated $E_v(x)$ at the two different mobility cases in Figs. 2(c) and 2(d) coalesce, suggesting that $\phi(x)$ is independent of mobilities in this case.

B. First-order approximation

In the case of finite mobilities $n(x) \approx n_0(x)$ and $p(x) \approx p_0(x)$ only within the high-density region near the cathode and anode contact, respectively, while the carrier densities strongly deviate from the ideal limit well inside the active layer, as shown in Figs. 2(a) and 2(b). The deviations $\Delta n(x)$ and $\Delta p(x)$ depend on both the light intensity and the charge-transport properties. In the low-intensity limit, however, when the second-order recombination term $\beta\Delta n\Delta p$ is negligible (the recombination rate is determined only by the first-order terms) and the space charge induced by Δn and Δp is insignificant [i.e., $F(x)$ is given by Eq. (20)], approximative solutions to Eqs. (12) and (13) can be obtained.

1. Drift-only solutions for $\Delta n(x)$

We consider the drift-only case, assuming the diffusion component of $\Delta n(x)$ to be negligible. For electrons sufficiently far from the cathode contact, the term $n_0(x)\Delta p(x)$ can be neglected. Then, noting that $p_0(x)$ is related to $F(x)$ via Eq. (18), in this region, Eq. (12) reduces to

$$-\mu_n F(x)\frac{\partial \Delta n}{\partial x} + [z_n - 1]\mu_n\frac{\partial F}{\partial x}\Delta n(x) = G_R, \tag{23}$$

where $G_R = G - \beta n_i^2[\exp(qV/kT) - 1]$ and $z_n = \beta/\beta_n$, with $\beta_n \equiv q\mu_n/(\varepsilon\varepsilon_0)$ being an equivalent electron-only Langevin recombination constant. The solution for Eq. (23) is of the form

$$\Delta n(x) = \frac{G_R}{\mu_n F_0}\frac{\int_0^x \tanh^{z_n}[(qF_0x'/2kT) + \sinh^{-1}(qF_0\lambda_{an}/2kT)]dx'}{\tanh^{z_n-1}[(qF_0x/2kT) + \sinh^{-1}(qF_0\lambda_{an}/2kT)]}, \tag{24}$$

with $\Delta n(0) = 0$ and using Eq. (20) for $F(x)$. An analogous expression can be obtained for $\Delta p(x)$ sufficiently far from the anode contact.

For the case of perfect Ohmic contacts (corresponding to $p_{an} \to \infty$ and $\lambda_{an} \to 0$), $\Delta n(x)$ far from both contacts simplifies as

$$J_n(x) \approx -q\mu_n F_0\Delta n(x) \approx -qG_R[x - x_{0n}], \tag{25}$$

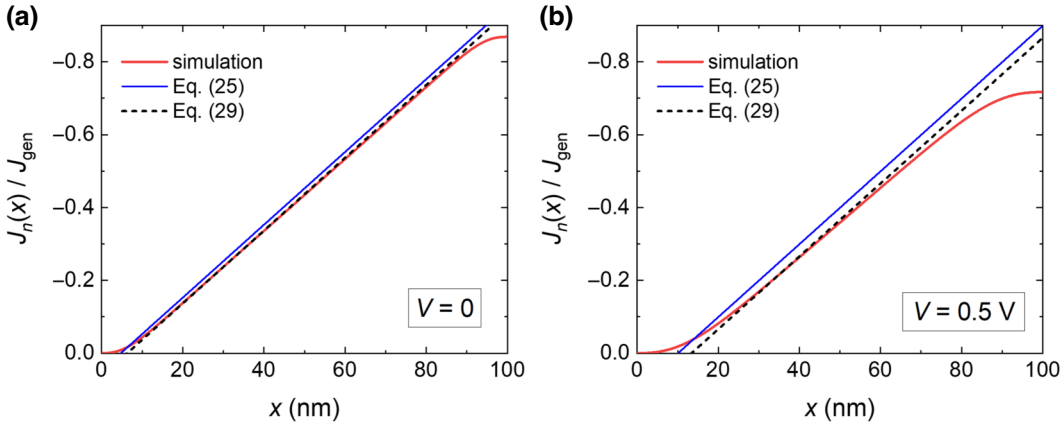

FIG. 3. Normalized electron current density profiles simulated at (a) short circuit and (b) $V = 0.5$ V for the low-mobility device from Fig. 1(b) ($\mu = 10^{-4}$ cm^2/V s and $\beta = \beta_L$), indicated by the red solid lines. The corresponding approximations Eqs. (25) and (29) for the electron current densities well inside the active layer are indicated by the solid blue lines and dashed lines, respectively.

where $x_{0n} = (kT/qF_0)f_0(\beta/\beta_n)$ with $f_0(z) \equiv 2\int_0^\infty [1 - \tanh^z(u)]du$. The integral function $f_0(z)$ can be readily evaluated for special cases (e.g., $f_0(2) = 2, f_0(1) = \ln(4)$); for a general z, we find

$$f_0(z) = \psi\left(\frac{z+1}{2}\right) + \gamma + \ln(4), \tag{26}$$

where ψ is the digamma function and $\gamma \approx 0.5772$ is the Euler constant. For $z \ll 1$ we expect $f_0(z) \to \pi^2 z/4$, while $f_0(z) \approx \ln[2z\exp(\gamma)]$ in the limit of large z. For practical purposes, however, it is convenient to assume the following approximation for Eq. (26):

$$f_0(z) \approx \ln\left(\sqrt{1 + B^2 z^2} + \frac{\pi^2 z}{4}\right), \tag{27}$$

with $B = [8\exp(\gamma) - \pi^2]/4 \approx 1.0947$, which reproduces the two extreme cases.

2. Accounting for diffusion

The preceding analysis culminating in Eq. (24) predicts that $J_n(x)$ is given by Eq. (25) far from the anode contact ($x \gg x_{0n}$). On the other hand, for $x < x_{0n}$, Eq. (24) approximates as

$$\Delta n(x) \approx \frac{qG_R x^2}{2\mu_n kT[1 + \beta/\beta_n]} \tag{28}$$

for perfect Ohmic contacts ($\lambda_{an} \to 0$). However, this treatment neglects diffusion of $\Delta n(x)$, assuming the drift component $\Delta J_{n,\text{drift}} = q\mu_n \Delta n F$ to be much larger than the corresponding diffusion component, $\Delta J_{n,\text{diff}} = \mu_n kT(\partial \Delta n/\partial x)$. While this is a good approximation for $x \gg x_{0n}$, the assumption is generally not valid for electrons close to the anode contact. Using Eq. (28), the corresponding $\Delta J_{n,\text{diff}}$ is approximately equal but opposite to the drift component ($\Delta J_{n,\text{diff}} \approx -\Delta J_{n,\text{drift}}$), suggesting the actual total electron current ($J_n = \Delta J_{n,\text{drift}} + \Delta J_{n,\text{diff}}$) for $x < x_{0n}$ is close to zero. Therefore, to a first approximation, the drift-only analysis underestimates the magnitude of $J_n(x)$ by $\Delta J_{n,\text{drift}}(x_{0n})$ for $x \gg x_{0n}$. Based on Eq. (28), we expect this correction to be given by $\Delta J_{n,\text{drift}}(x_{0n}) \approx -qG_R x_{0n}/(z_n + 1)$. A completely analogous consideration applies for $\Delta p(x)$. It should be stressed, however, that this approach is only applicable for large electric fields when the diffusion component of $\Delta n(x)$ inside the active layer is small compared with the associated drift component.

Based on these considerations, the electron and hole current densities well inside the active layer can then be approximated as

$$J_n(x) = -qG_R[x - x_{Rn}], \tag{29}$$

$$J_p(x) = qG_R[x - d + x_{Rp}]. \tag{30}$$

where $x_{Rn(p)} = (kT/qF_0)f_R(\beta/\beta_{n(p)})$, and $\beta_p = q\mu_p/(\varepsilon\varepsilon_0)$ is an equivalent hole-only Langevin recombination constant. Further, after approximating $f_0(z)$ by Eq. (27), $f_R(z)$ is given by

$$f_R(z) = \frac{z+2}{z+1} f_0(z) \approx \frac{z+2}{z+1} \ln\left(\sqrt{1 + B^2 z^2} + \frac{\pi^2 z}{4}\right). \tag{31}$$

Figure 3 shows the simulated $J_n(x)$ of the low-mobility device in Fig. 1(b) at low illumination conditions (where the first-order recombination channel dominates). Comparing the simulations with Eq. (29) yields a good agreement between the two inside the active layer.

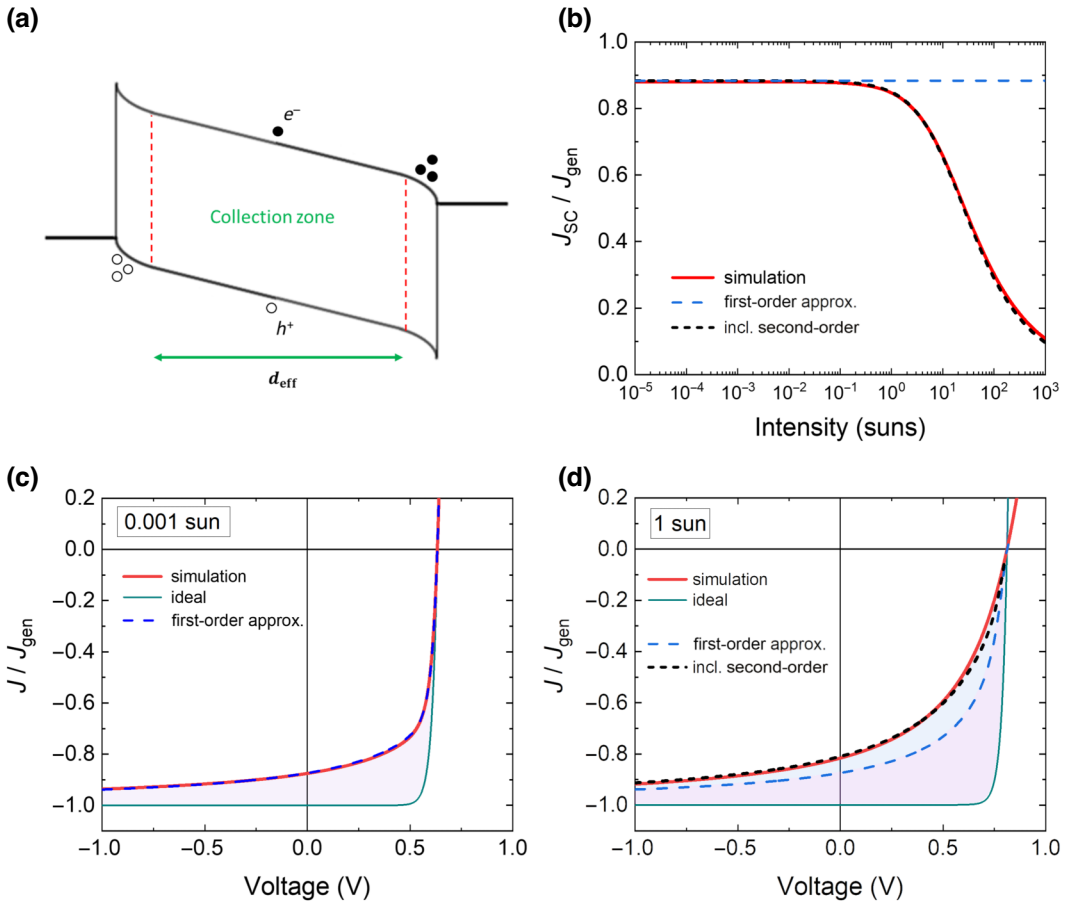

FIG. 4. (a) Schematic energy level diagram indicating the recombination zones near the contacts, where first-order recombination between injected and photogenerated carriers dominate, and the charge collection zone of width d_{eff} where first-order recombination is negligible. (b) Simulated intensity dependence of $J_{\text{SC}}/J_{\text{gen}}$ (red solid line) of the low-mobility device ($\mu = 10^{-4}$ cm^2/V s) from Fig. 1 is shown alongside the corresponding analytical approximations based on Eq. (33) (blue dashed line) and Eq. (41) (black dotted line). (c),(d) The corresponding simulated J-V curves at 0.001 sun [from Fig. 1(b)] and 1 sun [from Fig. 1(a)], respectively, indicated by red solid lines. The analytical approximations based on Eq. (33) (accounting for first-order recombination with injected carriers) and Eq. (41) (also including effects of second-order recombination among photogenerated carriers) are indicated by blue dashed and black dotted lines, respectively. The associated contributions from first- and second-order recombination to the total charge collection losses, relative to the ideal limit [Eq. (17), dark-cyan solid lines], are highlighted by purple and blue shaded areas, respectively.

3. Approximate expression for the current density

As is implied in Fig. 3, the effect of injected carriers is to induce recombination zones for minority carriers near the contacts. In accordance with Eqs. (29) and (30), x_{Rn} and x_{Rp} can be viewed as the corresponding effective widths within which all minority carriers recombine near the anode and cathode contact, respectively. Further, these recombination zones are separated by a recombination-free charge collection zone of width

$$d_{\text{eff}} = d - x_{Rn} - x_{Rp} \tag{32}$$

inside the active layer, as illustrated in the schematic energy level diagram in Fig. 4(a). Note that the widths of the recombination zones depend on the ratios between the mobilities and recombination coefficient and grow with increasing applied voltage. As a result, the recombination-free charge collection zone is reduced with increasing voltage, giving rise to an increased charge collection loss. Conversely, in the limit of large reverse-bias voltages, high mobilities, or small β, we expect $d_{\text{eff}} \to d$, as the ideal high-mobility limit is approached.

Finally, combining Eqs. (29) and (30), the total current density $J = J_n(x) + J_p(x)$, evaluated inside the active layer, can be approximated as

$$J(V) = \left(1 - \frac{\theta kT}{qF_0(V)d}\right) J_{\text{ideal}}(V), \tag{33}$$

where $J_{\text{ideal}}(V)$ is given by Eq. (17) and

$$\theta = f_R(\beta/\beta_n) + f_R(\beta/\beta_p). \tag{34}$$

with $f_R(z)$ defined through Eq. (31). Subsequently, the effect of a finite mobility is to reduce the magnitude of the current density, relative to the idealized high-mobility limit [Eq. (17)], by a prefactor given by d_{eff}/d. In addition to the applied voltage and the (effective) built-in voltage (via F_0), this current reduction factor only depends on β/β_n and β/β_p in the active layer (through θ).

Equation (33) generally describes the current density under low intensity conditions when first-order recombination with injected carriers dominates. In Fig. 4 the light-intensity dependence of $J_{\text{SC}}/J_{\text{gen}}$ of the low-mobility case from Fig. 1 ($\mu = 10^{-4}$ cm^2/Vs), along with the corresponding J-V curves at 0.001- and 1-sun conditions, is simulated and compared with the analytical prediction Eq. (33). Indeed, a nearly perfect agreement between Eq. (33) and the simulations is obtained at low intensities (0.001 sun). Note that for the case $\mu \to \infty$, Eq. (33) reduces back to the ideal-diode equation $J_{\text{ideal}}(V)$.

C. Accounting for second-order recombination between photogenerated carriers

As is evident from Fig. 4, a deviation between the simulations and the prediction based on Eq. (33) eventually appears at high enough intensities as second-order recombination between photogenerated electrons and holes becomes important. Under these conditions, the $\beta\Delta n\Delta p$ term in Eq. (12) can no longer be neglected. Subsequently, there will be a competition between charge extraction and second-order recombination taking place within the bulk of the active layer, with $J(V)$ deviating from Eq. (33). However, a correction to Eq. (33) can be obtained by accounting for second-order recombination within the charge collection zone, $x_{Rn} < x < d - x_{Rp}$. Since $\Delta n \gg n_0$ and $\Delta p \gg p_0$, within this region, Δn and Δp represent the actual excess densities of electrons and holes induced by photogeneration. First-order recombination (dominating near the contacts) is accounted for by assuming that $J_n(x_{Rn}) = 0$ and $J_p(d - x_{Rp}) = 0$. In other words, the device is effectively treated as having a thickness d_{eff}, where all electrons (holes) photogenerated within $0 < x < x_{Rn}$ ($d - x_{Rp} < x < d$) are lost due to recombination.

1. *Effect of second-order recombination inside the collection zone*

We consider the effect of second-order recombination at small voltages when $V_{\text{OC}} - V \gg kT/q$, corresponding to $G_R \approx G$. Then, assuming that the transport of photogenerated carriers is dominated by drift and that space-charge effects are negligible, within the charge collection zone, Eq. (12) simplifies as

$$-\mu_n F\frac{\partial \Delta n}{\partial x} = G - \beta\Delta n(x)\Delta p(x) = G - \frac{\beta J}{q\mu_p F}\Delta n(x) + \frac{\mu_n\beta}{\mu_p}\Delta n(x)^2, \quad (35)$$

where $J = q[\mu_n\Delta n(x) + \mu_p\Delta p(x)]F$ is used in the last step to eliminate $\Delta p(x)$. Assuming that $\Delta n(x_{Rn}) = 0$, while noting that the total current J is independent of x, Eq. (35) can be readily solved for $\Delta n(x)$ with the result

$$\Delta n(x) = \sqrt{\frac{\mu_p G}{\mu_n\beta}}\sqrt{1-\left(\frac{J}{J_\beta}\right)^2}\tan\left(2\sqrt{1-\left(\frac{J}{J_\beta}\right)^2}\frac{qG[x-x_{Rn}]}{J_\beta} + \sin^{-1}\left(\frac{J}{J_\beta}\right)\right) + \frac{J}{2q\mu_n F}, \quad (36)$$

for $x_{Rn} < x < d - x_{Rp}$, where $J_\beta = 2q\sqrt{\mu_n\mu_p}\sqrt{(G/\beta)}|F|$. An analogous treatment applies for photogenerated holes within the collection zone; in fact, assuming that $\Delta p = 0$ at $x = d - x_{Rp}$, it can be shown that $\Delta p(x) = (\mu_n/\mu_p)\Delta n(d - x_{Rp} - x)$.

Unfortunately, an analytically tractable explicit solution of Eq. (36) in terms of the total current density J cannot be established [17]. However, noting that $\mu_n\Delta n = \mu_p\Delta p$ (and thus $J_n = J_p = J/2$) at the midplane of the charge collection zone, the following implicit relation is obtained:

$$\sin^{-1}\left(\frac{J}{J_\beta}\right) = -\frac{J^*_{\text{gen}}}{J_\beta}\sqrt{1-\left(\frac{J}{J_\beta}\right)^2}. \quad (37)$$

Here, J^*_{gen} is defined as $J^*_{\text{gen}} = qGd_{\text{eff}}$ and corresponds to the magnitude of the current density obtained when all carriers photogenerated within the collection zone are extracted.

We note that the derivation of Eq. (36) assumes the electric field to be uniform in the charge collection zone. At small voltages, the electric field within this region is well approximated by $F \approx -F_0$. However, the derivation of Eq. (36) also neglects the effect of diffusion of photogenerated carriers induced by superlinear density profiles in the collection zone, resulting in Eq. (37) overestimating the magnitude of the actual J. The deviation may be estimated from the difference between the expected diffusion components $(\mu_n kT\partial\Delta n(x)/\partial x)$ of Eq. (36)

evaluated at the edge ($x = x_{Rn}$) and midplane of the collection zone. It turns out that this effect can be corrected for in Eq. (37) by modifying J_β as [43]

$$J_\beta \approx 2q\sqrt{\mu_n\mu_p}\sqrt{\frac{G}{\beta}}F_0\left[1+\frac{2kT}{qF_0d_{\text{eff}}}\right]^{-1/2}, \tag{38}$$

where the final term on the right-hand side of Eq. (38) represents a second-order correction induced by a diffusion of $\Delta n(x)$ in the collection zone.

In accordance with Eq. (37) the current density depends on the ratio J^*_{gen}/J_β, as shown in Fig. 5. As expected, J approaches $-J^*_{\text{gen}}$ in the limit when $J^*_{\text{gen}} \ll J_\beta$, corresponding to the low-intensity limit when second-order recombination within the charge collection zone is negligible. At high intensities when $J^*_{\text{gen}} \gg J_\beta$, in turn, Eq. (37) predicts that $J \to -J_\beta$; in this regime, the current is strongly limited by second-order bimolecular recombination between photogenerated electrons and holes inside the collection zone. For the general case, an explicit approximation for J can be obtained based on expanding the left-hand-side of Eq. (37) as $\sin^{-1}(J/J_\beta) \approx J/J_\beta$. Subsequently, the following approximative expression is found:

$$J \approx -\frac{J^*_{\text{gen}}}{\sqrt{1+K(V)}}, \tag{39}$$

with

$$K(V) = \left(\frac{J^*_{\text{gen}}}{J_\beta}\right)^2 + \kappa\frac{J^*_{\text{gen}}}{J_\beta}, \tag{40}$$

where κ is a correction factor. Here, the case $\kappa = 0$ corresponds to the first-order approximation $\sin^{-1}(J/J_\beta) \approx J/J_\beta$ in Eq. (37). However, by introducing an additional correction term (with nonzero κ), the accuracy between the exact value for J based on Eqs. (37) and (39) can be further improved. As shown in Fig. 5, a good agreement is obtained for $\kappa = 0.173$.

2. Revised approximation for the current density

Based on Eq. (39), Eq. (33) can be extended to account for the effect of second-order recombination among photogenerated charge carriers. Noting that J^*_{gen} is equal to Eq. (33) for $V_{\text{OC}} - V \gg kT/q$, it becomes evident that the effect of second-order recombination is to reduce the current density by a factor $1/\sqrt{1+K(V)}$. Hence, the current density can be approximated as

$$J(V) = \frac{1}{\sqrt{1+K(V)}}\left(1-\frac{\theta kT}{qF_0(V)d}\right)J_{\text{ideal}}(V). \tag{41}$$

In other words, apart from the reduction induced by recombination with injected carriers at the contacts, the magnitude of the current density is further reduced, relative to $J_{\text{ideal}}(V)$, by an additional reduction factor induced by second-order recombination among photogenerated carriers within the charge collection zone.

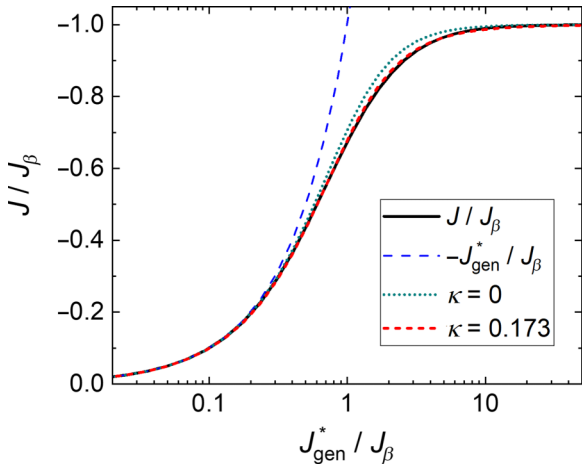

FIG. 5. Calculated J/J_β as a function of J^*_{gen}/J_β. The solid line corresponds to the exact (implicit) solution to Eq. (37). The approximations based on Eq. (39) with $\kappa = 0$ and $\kappa = 0.173$ are indicated by dotted and short-dashed lines, respectively. The case of $J = -J^*_{\text{gen}}$ (long-dashed lines) neglecting second-order recombination between photogenerated carriers has been included for comparison.

In accordance with Eq. (41), the current loss induced by second-order recombination among photogenerated carriers depends on the generation rate (or J_{gen}) with the magnitude of J/J_{gen} generally decreasing with increasing light intensity. Indeed, Eq. (41) reproduces both the simulated intensity dependence of $J_{\text{SC}}/J_{\text{gen}}$ and the J-V curve at 1 sun as shown in Figs. 4(b) and 4(d), respectively. The degree of second-order recombination is critically determined by K as per Eq. (40); at short-circuit, Eq. (40) can be approximated by

$$K \approx \frac{\beta G d^4}{4\mu_n\mu_p V_{\text{BI}}^2}\left(1-\frac{\theta kT}{qV_{\text{BI}}}\right)^2. \tag{42}$$

With the exception of the additional factor within the parenthesis, Eq. (42) is essentially identical to the figure-of-merit previously proposed by Bartesaghi *et al.* [10].

Apart from the photogeneration current (J_{gen}), the degree of the second-order recombination also depends on the recombination coefficient and the product of the electron and hole mobility. When $K \ll 1$, corresponding to low intensities, small β, or high enough mobilities, Eq. (41) reduces to Eq. (33) as the second-order recombination within the collection zone is negligible. Conversely, in the high-intensity regime, when $K \gg 1$, second-order recombination dominates over charge extraction of the photogenerated charge carriers. In this regime, J approaches a linear V dependence while displaying a sublinear intensity

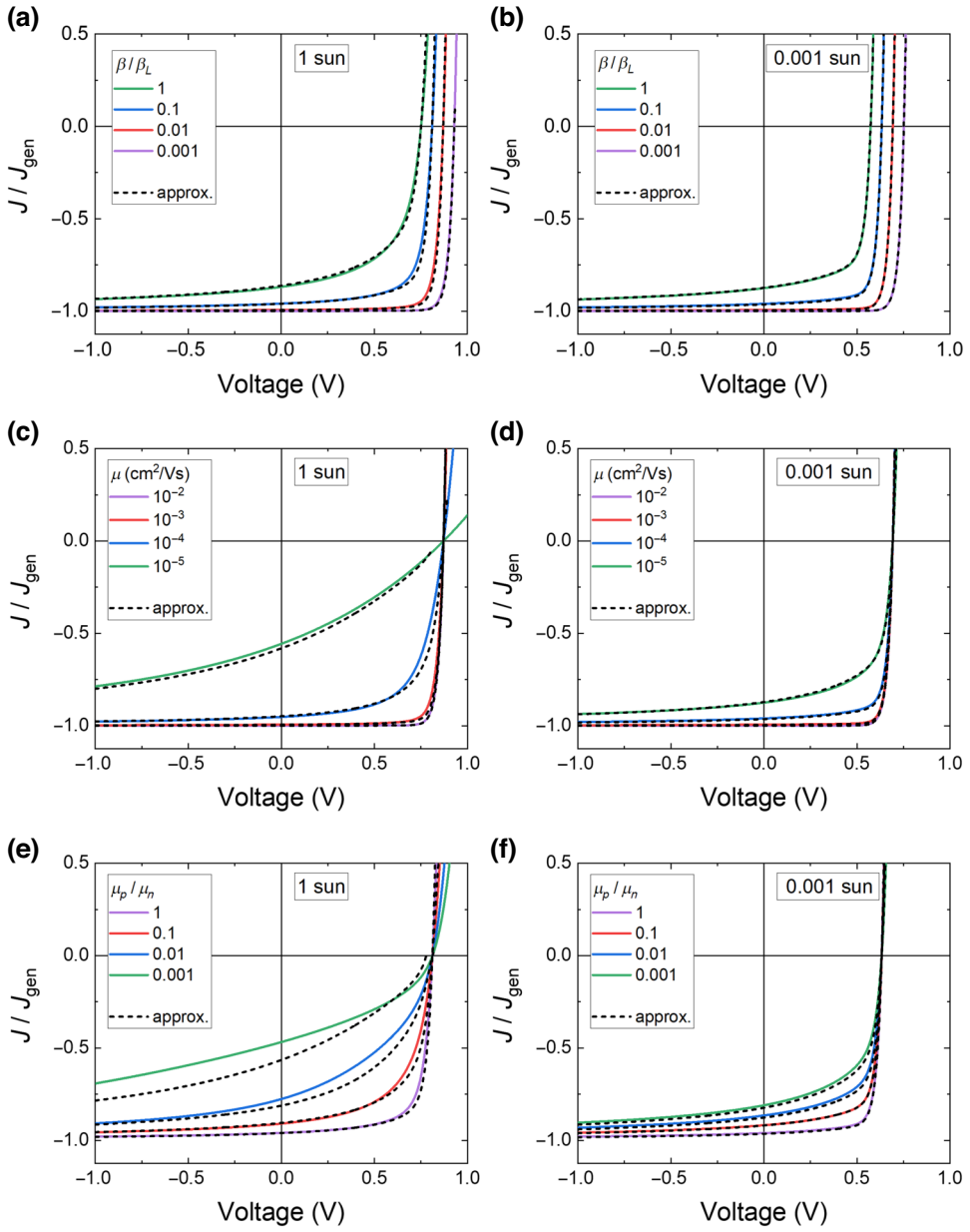

FIG. 6. Comparison between numerical simulations indicated by the colored solid lines and the analytical approximations Eq. (41) indicated by the corresponding dashed lines are shown under 1-sun (left-hand-side panel) and 0.001-sun (right-hand-side panel) illumination conditions. In (a),(b) the simulated J-V characteristics for the case of varying β/β_L are shown for $\mu_n = \mu_p = 10^{-3}$ cm^2/V s. In (c),(d) the simulated J-V characteristics at different but balanced mobilities are shown for $\beta = 10^{-11}$ cm^3/s. In (e),(f) the simulated J-V characteristics at increasing mobility imbalance μ_p/μ_n are shown for a fixed $\mu_n = 10^{-3}$ cm^2/V s and constant $\beta = 10^{-10}$ cm^3/s.

dependence of the form $J \propto G^{1/2}$ (or $J/J_{\rm gen} \propto G^{-1/2}$), consistent with previous reports [17,44,45].

D. Validation of the analytical model

To substantiate the presented analytical framework for the current density, we next compare the obtained diode equation [Eq. (41)] against numerical simulations of different cases. Figure 6 shows the numerically simulated J-V characteristics for varying mobilities β and mobility imbalance μ_p/μ_n under 1-sun and 0.001-sun illumination conditions. Upon comparing the numerically simulated J-V curves (colored solid lines) with the predictions based on Eq. (41) (black dashed lines) an excellent agreement is obtained for voltages sufficiently below $V_{\rm BI}$, in case of balanced mobilities. This is particularly true for the low-intensity cases (when $V_{\rm OC} \ll V_{\rm BI}$) where a virtually perfect agreement is obtained across the board.

At higher forward-bias voltages, however, a deviation is obtained for systems with low mobilities and large V_{OC}. This can be attributed to the fact that the approximation for F_0 [Eq. (21)] in Eq. (41) is no longer valid at high voltages [and that Eq. (41) diverges for $d_{eff} \to 0$]. In addition, effects of diffusion become increasingly important as the voltage approaches V_{BI}. This is expected to cause deviations near open circuit when V_{OC} becomes comparable to V_{BI}. Note that Eq. (41) is essentially indistinguishable from Eq. (33) at 0.001 sun, but also at 1 sun for mobilities $>10^{-3}$ cm^2/V s in Fig. 6.

A good agreement is also obtained for imbalanced mobilities, especially at low intensities. At large enough mobility imbalances, however, a deviation is eventually observed between the analytically predicted and the simulated *J-V* curves. This deviation is attributed to the inevitable space-charge build-up of the slower photogenerated carriers at high intensities, which screens the electric field inside the active layer, resulting in strongly space-charge-limited photocurrents [46–50].

E. Implications for photovoltaic device performance

The presented theoretical framework implies that the charge collection loss induced by bimolecular recombination can generally be partitioned into zeroth-, first-, and second-order contributions. The zeroth-order case [Eq. (17)] represents perfect charge collection of photogenerated carriers, containing only fundamental losses associated with the V_{OC}. Conversely, first- and second-order losses directly reduce the number of collected photogenerated carriers. The corresponding contributions from first- and second-order losses are highlighted by shaded areas in Figs. 4(c) and 4(d) for the case $\mu = 10^{-4}$ cm^2/V s. These results suggest that even at 1 sun the predominant charge collection loss due to bimolecular recombination in thin-film PVs (with Ohmic contacts) is first-order, while second-order losses only show up at low mobilities, which may not be relevant to state-of-the art devices. The implications of first-order charge collection losses for photovoltaic devices are discussed in the following.

1. Fill factor and power-conversion efficiency

For a solar cell under a given light intensity (I_L), the power-conversion efficiency (PCE) and FF are defined through $\mathrm{PCE} = |J(V_{MP})V_{MP}|/I_L = \mathrm{FF} \times J_{SC}V_{OC}/I_L$, where V_{MP} is the voltage at which the output power of the device is maximal. In the ideal-diode limit, when $J(V)$ is given by Eq. (17), the FF can be approximated as [25]

$$\mathrm{FF}_{\mathrm{ideal}} = \frac{(qV_{OC}/kT) - \ln(1 + (qV_{OC}/kT))}{1 + (qV_{OC}/kT)}, \tag{43}$$

with the corresponding maximum power point voltage given by

$$V_{MP}^{\mathrm{ideal}} = V_{OC} - \frac{kT}{q}\ln\left(1 + \frac{qV_{OC}}{kT}\right). \tag{44}$$

Equation (43) corresponds to the FF in the limit of ideal charge collection.

In the general case, the FF also depends on the interplay between μ_n, μ_p, and β, deviating from the ideal-diode limit set by Eq. (43). This is demonstrated in Fig. 7(a), where the FF is shown as a function of β/β_L for a wide set of numerically simulated devices with different μ_n, μ_p, β, and J_{gen}, while keeping the V_{OC} fixed at either 0.81 or 0.63 V. The mobilities are allowed to vary independently across 6 orders of magnitude from 10^{-7} to 10^{-1} cm^2/V s. As shown, there is a large spread in the simulated data. While the upper bound of the FF is seen to correlate with β/β_L, approaching Eq. (43) at small β/β_L, the lower bound remains largely independent of β/β_L. Previous studies have suggested the FF to depend critically on $\beta J_{gen}/(\mu_n\mu_p)$ [10,11], encapsulated in the figure-of-merit α proposed by Neher *et al.* [15],

$$\alpha^2 = \frac{q\beta J_{gen}d^3}{4\mu_n\mu_p(kT)^2}. \tag{45}$$

Such a dependence is expected when the photocurrent is limited by second-order recombination [cf. Equation (42)]. In Fig. 7(b), the numerically simulated FFs [from Fig. 7(a)] are replotted as a function of α. However, the spread in the FF remains substantial, especially for moderate α values. This observation suggests that first-order recombination with injected carriers plays a crucial role in determining the FF in this case.

An approximation of FF for the case when first-order recombination with injected carriers dominates can be obtained from Eq. (33). Noting that the principal voltage dependence in Eq. (33) is determined by the $J_{\mathrm{ideal}}(V)$ component, while the prefactor varies relatively slowly with voltage, we expect $V_{MP} \approx V_{MP}^{\mathrm{ideal}}$. Subsequently, the FF is reduced relative to the ideal limit by the ratio between the prefactor at $V = V_{MP}$ and at short circuit as follows:

$$\mathrm{FF} \approx \frac{\mathrm{FF}_{\mathrm{ideal}}}{(1 - (\theta kT/qV_{BI}))}\left(1 - \frac{\theta kT}{qF_0(V_{MP}^{\mathrm{ideal}})d}\right), \tag{46}$$

where $\mathrm{FF}_{\mathrm{ideal}}$ and V_{MP}^{ideal} are given by Eqs. (43) and (44), respectively. The critical material parameter determining FF in this case is θ, which depends on β/β_n and β/β_p in accordance with Eqs. (31) and (34); in the limit of small β

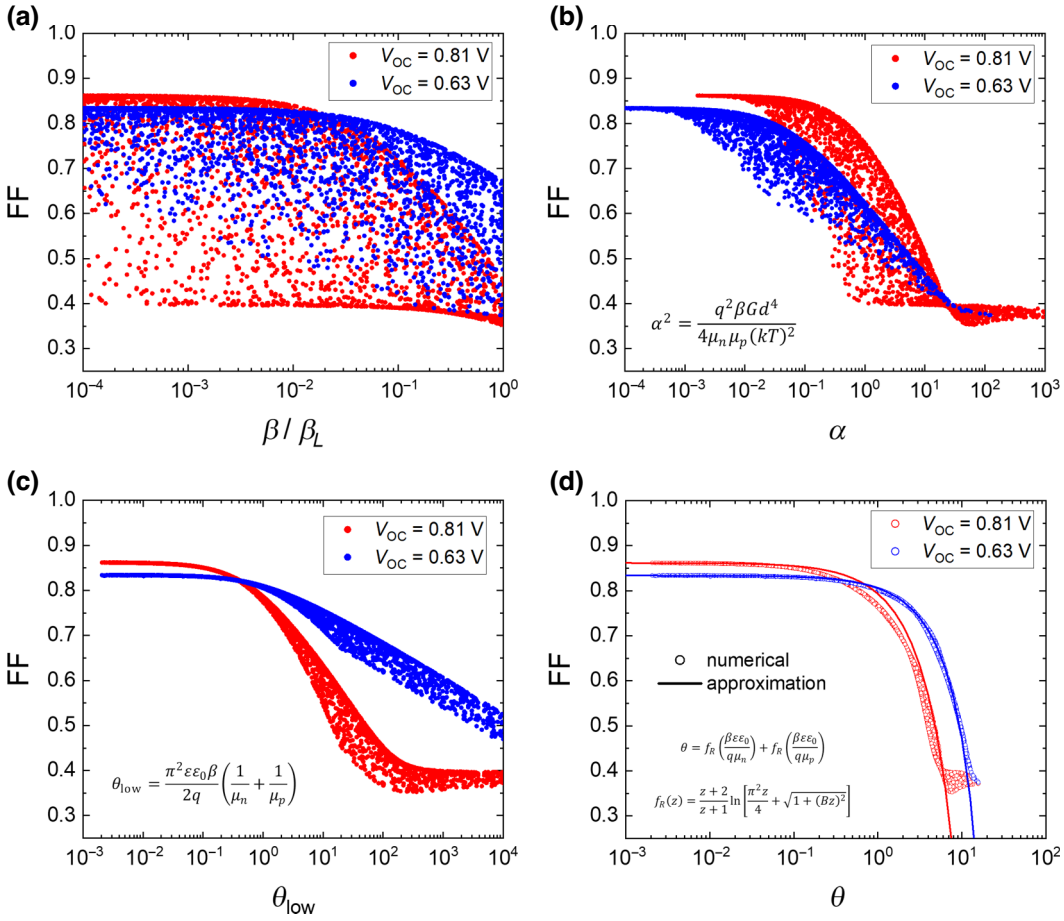

FIG. 7. The fill factor as a function of (a) β/β_L, (b) α, (c) θ_{low}, and (d) θ for a large set of numerically simulated devices (symbols) with different μ_n, μ_p, β/β_L, and G at fixed open-circuit voltages of $V_{\text{OC}} = 0.81$ V and $V_{\text{OC}} = 0.63$ V. In the simulations, β/β_L spans between 0.0001 and 1, while μ_n and μ_p are allowed to independently vary between 10^{-7} and 10^{-1} $\text{cm}^2/\text{V s}$. For comparison, the approximation based on Eq. (46) is included in panel (d) as indicated by solid lines, corresponding to the limit of the FF when the charge collection is limited by first-order recombination with injected carriers.

and large mobilities, θ can be approximated by

$$\theta_{\text{low}} = \frac{\pi^2 \beta}{2\beta_n} + \frac{\pi^2 \beta}{2\beta_p} = \frac{\pi^2 \varepsilon \varepsilon_0}{2q}\left[\frac{\beta}{\mu_n} + \frac{\beta}{\mu_p}\right]. \quad (47)$$

Hence, we expect FF to be limited by the ratio between the bimolecular recombination coefficient and the smaller mobility.

In Fig. 7(c), the simulated FFs [from Figs. 7(a) and 7(b)] are plotted as a function of θ_{low}. Indeed, a much better correlation is obtained in this case, suggesting that the simulated FFs in Fig. 7 are primarily governed by first-order recombination between injected and photogenerated charge carriers. This is further substantiated in Fig. 7(d), where, upon plotting the numerically simulated FFs (symbols) as a function of θ [obtained from Eq. (34)], the simulated data set is seen to coalesce into a common trend that depends only on θ. For comparison, the approximation based on Eq. (46) (solid lines) has been included in Fig. 7(d), showing an excellent agreement against the simulated FFs at small θ (large mobilities and/or small β) and low V_{OC}, in particular. Note that, for balanced mobilities, θ depends only on β/β_L explaining the behavior of the upper bound of FF in Fig. 7(a). The spread observed in Figs. 7(a) and 7(b) can thus be traced back to an increased mobility imbalance. A significant deviation from the trend in Fig. 7(d) is seen only for high V_{OC} at $\theta \gg 1$ (corresponding to severely imbalanced mobilities), when the simulated devices instead become limited by space-charge effects and second-order recombination. Based on these results, we see that the condition for a thin-film device to be in the high-mobility regime is that $\theta_{\text{low}} \ll 1$ or, equivalently, that $\mu \gg (\pi^2 \varepsilon \varepsilon_0 \beta / 2q)$ for the mobility of the slower charge-carrier type.

Equation (46) predicts a relatively weak dependence on the active layer thickness, with the d dependence being implicitly accounted for within the terms $F_0(V_{\text{MP}}^{\text{ideal}})d$ and V_{BI}. It should be stressed, however, that Eq. (46) is only valid for sufficiently thin devices. As the active layer thickness is increased, the device rapidly becomes

influenced by second-order recombination [not accounted for in Eq. (46)], which generally results in a strong d dependence in FF.

The findings in Fig. 7 have important implications not only for the FF, but also for the maximal achievable PCE in low-mobility solar cell devices. Combining Eq. (46) with the corresponding J_{SC} predicted by Eq. (33), an upper limit estimate of the PCE for low-mobility thin-film devices with Ohmic contacts can be established. The corresponding PCE takes the form

$$\mathrm{PCE} = \mathrm{PCE}_{\mathrm{ideal}}\left(1 - \frac{\theta kT}{qF_0(V_{\mathrm{MP}}^{\mathrm{ideal}})d}\right), \qquad (48)$$

where $\mathrm{PCE}_{\mathrm{ideal}}$ is the PCE expected in the case of perfect charge collection. The parameter θ may thus be taken as an associated figure-of-merit for charge collection. Figure 8 shows the $\mathrm{PCE}/\mathrm{PCE}_{\mathrm{ideal}}$ of the numerically simulated devices from Fig. 7 plotted as a function of θ. Again, for a given V_{OC} (and V_{BI}) the simulated data set coalesces into a common trend that depends only on θ. Indeed, comparing the simulated trend with the upper limit estimate Eq. (48), a very good overall agreement can be obtained. As a result, Eq. (48) can be used to separately estimate the loss in the PCE associated with charge collection in devices with selective Ohmic contacts. These results can also be used to facilitate machine learning for PCE predictions. The fact that the spread in the numerically simulated data (from Fig. 7) is drastically reduced when parametrized against θ elevates θ as a more accurate figure-of-merit for charge collection in thin-film PVs based on low-mobility semiconductors such as OPVs.

2. The dark current and the reciprocity between charge injection and extraction

The theoretical framework based on Eq. (33) can be consolidated with the principle of reciprocity between charge injection and extraction [51], provided that the voltage dependence of the photovoltaic external quantum efficiency (EQE) is accounted for [52]. In general, the EQE describes the efficiency of incident photons being converted into collected electron-hole pairs at the contacts. In excitonic semiconductors, the EQE can be written as $\mathrm{EQE} = \eta_{\mathrm{abs}}\eta_{\mathrm{CGY}}\eta_{\mathrm{col}}$, where η_{abs} is the efficiency of an incident photon being absorbed and generating an exciton, and η_{CGY} is the efficiency of a photogenerated exciton generating a free electron-hole pair. Finally, η_{col} is the charge collection efficiency of photogenerated carriers, defined as $\eta_{\mathrm{col}} = |J - J_{\mathrm{dark}}|/J_{\mathrm{gen}}$, where J_{dark} is the current density under dark conditions. Note that, from this perspective, J_{gen} can be equivalently expressed as $J_{\mathrm{gen}} = q\int_0^\infty \eta_{\mathrm{abs}}\eta_{\mathrm{CGY}}\Phi_{\mathrm{ext}}dE$, where $\Phi_{\mathrm{ext}}(E)$ is the photon flux of the external light source used to photogenerate charge carriers (e.g., 1 sun).

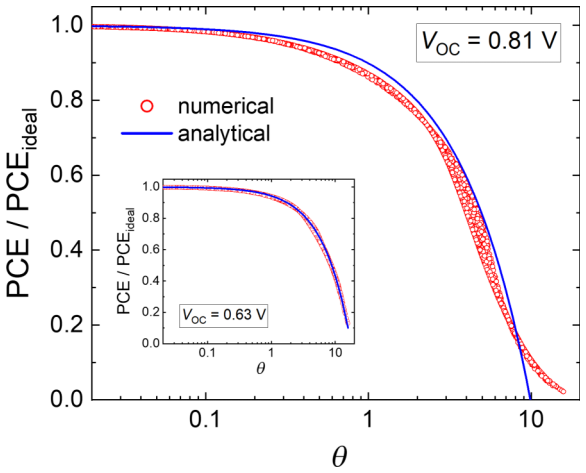

FIG. 8. The $\mathrm{PCE}/\mathrm{PCE}_{\mathrm{ideal}}$ of the numerically simulated devices from Fig. 7 are shown as a function of the figure-of-merit θ at $V_{\mathrm{OC}} = 0.81$ V, as indicated by open symbols. The corresponding case for $V_{\mathrm{OC}} = 0.63$ V is shown in the inset. The upper-limit estimate of the PCE based on Eq. (48), expected in the presence of first-order recombination with injected carriers, is depicted by the solid lines.

In accordance with Eq. (33), under conditions when recombination between photogenerated and injected charge carriers dominates, the charge collection efficiency is given by

$$\eta_{\mathrm{col}}(V) = 1 - \frac{\theta kT}{qF_0(V)d}, \qquad (49)$$

for $V \ll V_{\mathrm{BI}}$. Based on Eq. (49), η_{col} depends on the applied voltage but is independent of light intensity, consistent with the first-order nature of the current loss. In fact, Eq. (49) applies to dark conditions as well, noting that the current density of Eq. (33) in the dark is given by

$$J_{\mathrm{dark}}(V) = \left(1 - \frac{\theta kT}{qF_0(V)d}\right)J_0\left[\exp\left(\frac{qV}{kT}\right) - 1\right], \qquad (50)$$

for $V \ll V_{\mathrm{BI}}$.

The effect of finite mobilities is to reduce the injected dark current density, relative to the ideal-diode case $J_{\mathrm{ideal}} = J_0[\exp(qV/kT) - 1]$ [i.e., Eq. (17) in the dark], by the prefactor $\eta_{\mathrm{col}}(V)$ given by Eq. (49). Concomitantly, $J_{\mathrm{dark}}(V)$ can be described in terms of an effective dark saturation current density $J_{0,\mathrm{eff}}(V) = \eta_{\mathrm{col}}(V)J_0$, which depends on the applied voltage. This is demonstrated in Fig. 9, where J-V curves under dark conditions are simulated and compared to Eq. (50), showing excellent agreement for $V \ll V_{\mathrm{BI}}$. We note that the additional voltage dependence present at low mobilities translates into nonideal-diode behavior in the forward bias, which, depending on V, is seen as a diode ideality factor above unity in the dark.

A different situation applies at open circuit under illumination. Under open-circuit conditions, the rates of

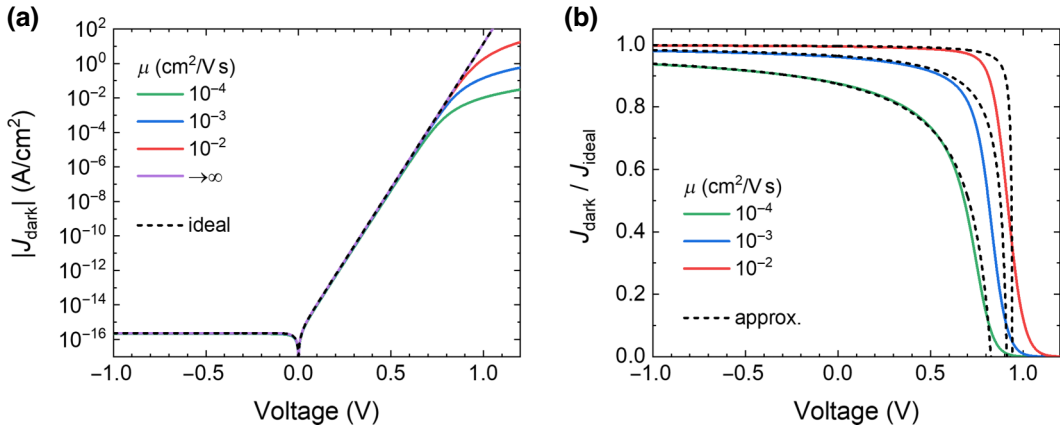

FIG. 9. (a) Simulated dark current densities at different mobilities with β of 10^{-10} cm^3/s. (b) Normalized dark current densities relative to the idealized expected dark current density [Eq. (17) with $J_{gen} = 0$] in the limit of high mobilities. The approximations based on Eq. (50) are indicated by dashed lines.

charge-carrier injection and extraction are exactly balanced ($J = 0$). From Eq. (17) [or Eq. (33)], the open-circuit voltage is obtained as

$$V_{OC} = \frac{kT}{q} \ln\left(1 + \frac{J_{gen}}{J_0}\right). \tag{51}$$

Since $J_n(x) = J_p(x) = 0$, corresponding to $\partial E_{Fn}/\partial x = \partial E_{Fp}/\partial x = 0$, the device is essentially operating in the ideal-diode regime under these conditions. For a fixed β (and light intensity), the V_{OC} is therefore independent of the charge-transport properties. This is seen in the simulated J-V curves in Figs. 6(c)–6(f), where V_{OC} remains unchanged with varying mobility. Note that Eq. (51) is equivalent to $J_{gen} = J_0[\exp(qV_{OC}/kT) - 1]$. Therefore, the ideal J-V curve [Eq. (17)] expected for a given device may be constructed from the corresponding $J_{gen} - V_{OC}$ curve, which can be obtained from intensity-dependent suns-V_{OC} measurements [53].

J_0 is defined as the (saturated) thermal generation current density in the bulk. Noting that charge carriers can be thermally generated either radiatively or nonradiatively, we can write $J_0 = (q/\eta_{rad}) \int_0^\infty \eta_{abs}\eta_{CGY}\Phi_{BB}dE$, where $\Phi_{BB}(E)$ is the black-body photon flux of the environment and η_{rad} is the radiation efficiency. On the other hand, provided that η_{col} remains independent of intensity, it follows that $J_{gen}/J_0 = \eta_{col}(V)J_{gen}/J_{0,eff}(V)$. If the EQE is evaluated at low intensities under short-circuit conditions ($V = 0$), Eq. (51) can then be reformulated as

$$V_{OC} = \frac{kT}{q} \ln\left(1 + \frac{J^*_{SC}}{J_{0,SC}}\right), \tag{52}$$

where $J^*_{SC} = q \int_0^\infty \mathrm{EQE}(E)\phi_{ext}(E)dE$ is the expected J_{SC} in the absence of second-order losses, while $J_{0,SC} = (q/\eta_{rad}) \int_0^\infty \mathrm{EQE}(E)\phi_{BB}(E)dE$ corresponds to $J_{0,eff}(V = 0)$, consistent with detailed balance.

Note that $J_{0,SC}$ generally differs from J_0, owing to the fact that η_{col}, and thus the EQE, generally depends on voltage. Indeed, such a voltage-dependent EQE (at low light intensity) was also experimentally observed by Würfel *et al.* [22]. In addition, it should be emphasized that the EQE-integrated short-circuit current density J^*_{SC} generally only equals the actual short-circuit current density J_{SC} for conditions when Eq. (42) is negligibly small, i.e., $K \ll 1$. For very low mobilities or high intensities, this condition is no longer valid, and a deviation from reciprocity is expected at open circuit, in agreement with previous findings [52].

F. Other effects

The presented diode equations neglect the effect of external resistive losses. In real devices, the voltage V over the active layer (diode) is generally different to the externally applied voltage V_{ext}, due to the finite resistance of the wires (connecting the load to the diode) and the electrodes. In addition, diode devices suffer from parasitic shunts, commonly attributed to extrinsic nonidealities from the device fabrication. The device-intrinsic current density $J(V)$ (considered previously) is related to the external current density J_{meas}, measured as a function of V_{ext}, via

$$J_{meas}(V_{ext}) = J(V) + \frac{V}{\mathcal{R}_{shunt}}, \tag{53}$$

where $V = V_{ext} - J_{meas}\mathcal{R}_{series}$. Here, $\mathcal{R}_{series}$ is the combined series resistance (in units of $\Omega\,\mathrm{cm}^2$) of the external circuit and the electrodes and $\mathcal{R}_{shunt}$ is the shunt resistance (in $\Omega\,\mathrm{cm}^2$). While voltage losses induced by a finite series resistance become prevalent when the magnitude of the current density is large (high intensity and/or high forward bias), the effect of the shunt is generally important at low current densities and light intensities (dominating the measured dark current density in the reverse bias).

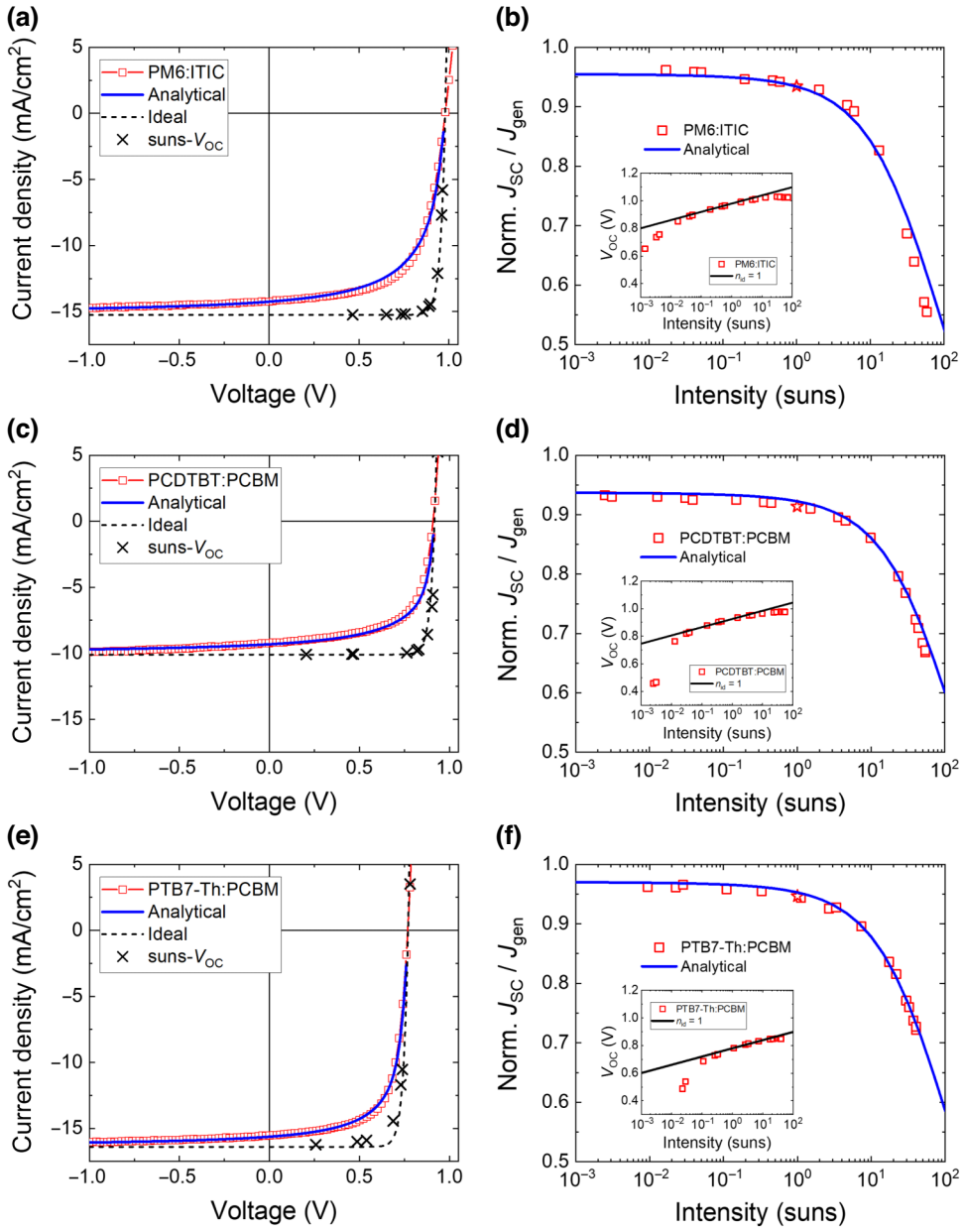

FIG. 10. (a) Experimental J-V curves at 1 sun and (b) normalized J_{SC}/J_{gen} as a function of light intensity for PM6:ITIC are shown (symbols). (c),(d) are a repetition of panels (a),(b) for PCDTBT:PCBM. (e),(f) are a repetition of panels (a),(b) for PTB7-Th:PCBM. Star-shaped symbols indicate the value at 1 sun. The corresponding suns-V_{OC} measurements are shown as insets. The solid lines indicate the qualitative fits using Eq. (41). Corresponding ideal J-V curves as predicted by the analytical model (dashed lines) and by the suns-V_{OC} measurements (crosses) have been included for comparison.

The presented theoretical treatment for $J(V)$ applies to undoped thin-film diode devices with Ohmic contacts, dominated by bimolecular recombination. This corresponds to situations where additional loss channels induced by trap-assisted recombination and surface recombination of minority carriers at the contacts are negligible. In accordance with Eq. (51), we expect the light ideality factor n_{id}, defined through $qV_{OC} \propto n_{id}kT\ln(J_{gen})$, to equal unity ($n_{id} = 1$) under such conditions.

If there is a sufficiently large number of traps in the active layer, however, the resultant trap-assisted recombination generally gives rise to an increased charge collection loss [45,54–57], which depends on the trap energy and distribution. Similar to doping in the active layer [58], trapped charge carriers may also induce considerable electric field screening inside the active layer [55,59], further reducing the photocurrent. The presence of trap-assisted recombination is generally manifested by

a light ideality factor above unity, $n_{id} > 1$. Similarly, if the contacts are nonselective for the extraction of majority carriers, additional charge collection losses and reductions in the open-circuit voltages caused by surface recombination of minority carriers may occur. This loss is expected to be particularly prominent in case of energetically unoptimized contacts and/or large carrier mobilities [60–63], and commonly correlates with an ideality factor below unity, $n_{id} < 1$.

Finally, it should be stressed that the theoretical analysis is limited to thin active layers with relatively uniform charge-carrier generation rates. While the absorption rate of photons inside the active layer decays exponentially with the distance from the transparent electrode, the combined effect of optical interference and back reflection from the reflective counter electrode results in smooth generation rates in (optically) thin active layers. For thick active layers, however, the photon absorption rate in the active layer is concentrated near the transparent contact resulting in a highly nonuniform charge-carrier generation and asymmetric charge extraction [64–67]. Furthermore, thick active layers are generally more sensitive to space-charge effects induced by photogenerated carriers, trapped charge carriers, or (unintentional) dopants.

G. Comparison with experimental data

To test the validity against experimental data, we applied our analytical model to three different OPV systems where bimolecular recombination is the dominant loss mechanism of photogenerated charge carriers: poly[(2,6-(4,8-bis(5-(2-ethylhexyl-3-fluoro)thiophen-2-yl)-benzo[1,2-b:4,5-b′]dithiophene))-alt-5,5-(1′,3′-di-2-thienyl-5′,7′-bis(2-ethylhexyl)benzo[1′,2′-c:4′,5′-c′]dithiophene-4,8-dione)]:3,9-bis(2-methylene-(3-(1,1-dicyanomethylene)-indanone))-5,5,11,11-tetrakis(4-hexylphenyl)-dithieno[2,3-d:2′,3′-d′]-s-indaceno[1,2-b:5,6-b′]dithiophene (PM6:ITIC); poly[N-9′-heptadecanyl-2,7-carbazole-alt-5,5-(4′,7′-di-2-thienyl-2′,1′,3′-benzothiadiazole)]:[6,6]-phenyl-C71-butyric acid methyl ester (PCDTBT:PCBM); and poly[4,8-bis(5-(2-ethylhexyl)thiophen-2-yl)benzo[1,2-b;4,5-b′]dithiophene-2,6-diyl-alt-(4-(2-ethylhexyl)-3-fluorothieno[3,4-b]thiophene-)-2-carboxylate-2-6-diyl]:PCBM (PTB7-Th:PCBM). The carrier mobilities in these systems were previously found to be balanced and estimated to be close to 2×10^{-4} cm^2/Vs for PM6:ITIC and PTB7-Th:PCBM, and 10^{-4} cm^2/Vs for PCDTBT:PCBM. The details of the device fabrication and the experimental measurements can be found elsewhere [68,69].

In Fig. 10, the J-V curves under 1-sun illumination (left panel) and light-intensity-dependent J_{SC}/J_{gen} (right panel) of PM6:ITIC [Figs. 10(a) and 10(b)], PCDTBT:PCBM [Figs. 10(c) and 10(d)], and PTB7-Th:PCBM [Figs. 10(e) and 10(f)] are shown and indicated by open symbols. The corresponding suns-V_{OC} data have been included as insets in Fig. 10. The presence of bimolecular recombination in these systems is evident from the pronounced intensity dependence of J_{SC}/J_{gen}, consistent with second-order recombination prevailing at the higher intensities (above 1 sun), and the observed suns-V_{OC} dependence following a light ideality factor of $n_{id} = 1$ (in the relevant intensity regime). The drastic decrease in V_{OC} at lower intensities near and below 0.01 sun (while J_{SC}/J_{gen} remains unaffected) can be attributed to shunt effects starting to dominate, as per Eq. (53).

The solid lines in Fig. 10 indicate the qualitative fits based on Eq. (41) using β and V_{BI} as fitting parameters. An overall excellent agreement between the analytical model and the experimental data can be found. Herein, $\beta = 0.15\beta_L \approx 3.6 \times 10^{-11}$ cm^3/s for PM6:ITIC; $\beta = 0.25\beta_L \approx 3 \times 10^{-11}$ cm^3/s for PCDTBT:PCBM; and $\beta = 0.07\beta_L \approx 1.7 \times 10^{-11}$ cm^3/s for PTB7-Th:PCBM. The relatively large values for β/β_L are consistent with the moderate FFs in these systems. The deviation between the experimental data and the fit at the highest intensities in Fig. 7(b) is attributed to additional losses induced by the series resistance of the external circuit (cf. Sec. III F). The corresponding ideal J-V curves (perfect collection) predicted by the analytical model are depicted by the dashed lines in Fig. 10 (left panel). For comparison, the reconstructed ideal J-V curves based on the experimental suns-V_{OC} data have also been included as indicated by crosses. As expected, a good agreement is again obtained. These results further fortify the validity of the analytical model.

IV. CONCLUSIONS

In conclusion, we present an analytic framework for describing the device physics of charge collection in thin-film PVs with Ohmic contacts and limited by bimolecular recombination. Based on this framework, a diode equation describing the J-V characteristics is derived, showing excellent agreement with numerical drift-diffusion simulations. The presented framework is further employed to analytically understand what limits the charge collection efficiency, FF, and ultimately the PCE in sandwich-type thin-film PVs based on low-mobility semiconductors, including organic solar cells and photodiodes. The obtained findings provide vital physical insights into the interplay between charge-carrier extraction, injection, and bimolecular recombination and their influence on the device performance. In addition, the derived approximations can be used to extract material parameters from experimental data, for example, using a global fitting procedure, in systems where bimolecular recombination is the dominant loss mechanism of photogenerated charge carriers.

ACKNOWLEDGMENTS

This work was partially funded by the UKRI through the EPSRC Program Grant No. EP/T028513/1 Application Targeted and Integrated Photovoltaics. O.J.S. acknowledges funding from the Research Council of Finland through Project No. 357196.

[1] T. D. Lee and A. U. Ebong, A review of thin film solar cell technologies and challenges, Renewable Sustainable Energy Rev. **70**, 1286 (2017).

[2] B. Kippelen and J. L. Brédas, Organic photovoltaics, Energy Environ. Sci. **2**, 251 (2009).

[3] S. M. Sze, *Physics of Semiconductor Devices*, 3rd ed. (Wiley & Sons, New York, 1981).

[4] T. Kirchartz, J. Bisquert, I. Mora-Sero, and G. Garcia-Belmonte, Classification of solar cells according to mechanisms of charge separation and charge collection, Phys. Chem. Chem. Phys. **17**, 4007 (2015).

[5] W. Tress, *Organic Solar Cells: Theory, Experiment, and Device Simulation* (Springer International Publishing, Cham, 2014).

[6] U. Würfel, D. Neher, A. Spies, and S. Albrecht, Impact of charge transport on current–voltage characteristics and power-conversion efficiency of organic solar cells, Nat. Commun. **6**, 6951 (2015).

[7] T. Kirchartz, P. Kaienburg, and D. Baran, Figures of merit guiding research on organic solar cells, J. Phys. Chem. C **122**, 5829 (2018).

[8] A. Armin, W. Li, O. J. Sandberg, Z. Xiao, L. Ding, J. Nelson, D. Neher, K. Vandewal, S. Shoaee, T. Wang, *et al.*, A history and perspective of non-fullerene electron acceptors for organic solar cells, Adv. Energy Mater. **11**, 20003570 (2021).

[9] C. L. Cutting, M. Bag, and D. J. Venkataraman, Indoor light recycling: A new home for organic photovoltaics, J. Mater. Chem. C **4**, 10367 (2016).

[10] D. Bartesaghi, I. del Carmen Pérez, J. Kniepert, S. Roland, M. Turbiez, D. Neher, and L. J. A. Koster, Competition between recombination and extraction of free charges determines the fill factor of organic solar cells, Nat. Commun. **6**, 7083 (2015).

[11] P. Kaienburg, U. Rau, and T. Kirchartz, Extracting information about the electronic quality of organic solar-cell absorbers from fill factor and thickness, Phys. Rev. Appl. **6**, 024001 (2016).

[12] C. M. Proctor, M. Kuik, and T.-Q. Nguyen, Charge carrier recombination in organic solar cells, Prog. Polym. Sci. **38**, 1941 (2013).

[13] R. S. Crandall, Transport in hydrogenated amorphous silicon p-i-n solar cells, J. Appl. Phys. **53**, 3350 (1982).

[14] K. Taretto, New explicit current/voltage equation for p-i-n solar cells including interface potential drops and drift/diffusion transport, Prog. Photovoltaics **22**, 870 (2014).

[15] D. Neher, J. Kniepert, A. Elimelech, and L. J. A. Koster, A new figure of merit for organic solar cells with transport-limited photocurrents, Sci. Rep. **6**, 24861 (2016).

[16] M. L. I. Ibrahim, Z. Ahmad, and K. Sulaiman, Analytical expression for the current-voltage characteristics of organic bulk heterojunction solar cells, AIP Adv. **5**, 027115 (2015).

[17] D. R. B. Amorim, D. J. Coutinho, P. B. Miranda, and R. M. Faria, Analytical model for photocurrent in organic solar cells as a function of the charge-transport figure of merit including second-order recombination, Phys. Rev. Appl. **14**, 034046 (2020).

[18] C. Deibel, A. Wagenpfahl, and V. Dyakonov, Origin of reduced polaron recombination in organic semiconductor devices, Phys. Rev. B **80**, 075203 (2009).

[19] S. L. M. van Mensfoort and R. Coehoorn, Effect of Gaussian disorder on the voltage dependence of the current density in sandwich-type devices based on organic semiconductors, Phys. Rev. B **78**, 085207 (2008).

[20] P. de Bruyn, A. H. P. van Rest, G. A. H. Wetzelaer, D. M. de Leeuw, and P. W. M. Blom, Diffusion-limited current in organic metal-insulator-metal diodes, Phys. Rev. Lett. **111**, 186801 (2013).

[21] U. Würfel and M. Unmüssig, Apparent field-dependence of the charge carrier generation in organic solar cells as a result of (bimolecular) recombination, Sol. RRL **2**, 1800229 (2018).

[22] U. Würfel, L. Perdigón-Toro, J. Kurpiers, C. M. Wolff, P. Caprioglio, J. J. Rech, J. Zhu, X. Zhan, W. You, S. Shoaee, *et al.*, Recombination between photogenerated and electrode-induced charges dominates the fill factor losses in optimized organic solar cells, J. Phys. Chem. Lett. **10**, 3473 (2019).

[23] D. Padula, J. D. Simpson, and A. Troisi, Combining electronic and structural features in machine learning models to predict organic solar cells properties, Mater. Horiz. **6**, 343 (2019).

[24] N. Majeed, M. Saladina, M. Krompiec, S. Greedy, C. Deibel, and R. C. I. MacKenzie, Using deep machine learning to understand the physical performance bottlenecks in novel thin-film solar cells, Adv. Funct. Mater. **30**, 1907259 (2020).

[25] P. Würfel, *Physics of Solar Cells*, 2nd ed. (Wiley-VCH, Weinheim, Germany, 2009).

[26] C. Deibel and V. Dyakonov, Polymer-fullerene bulk heterojunction solar cells, Rep. Prog. Phys. **73**, 096401 (2010).

[27] L. J. A. Koster, E. C. P. Smits, V. D. Mihailetchi, and P. W. M. Blom, Device model for the operation of polymer/fullerene bulk heterojunction solar cells, Phys. Rev. B **72**, 085205 (2005).

[28] D. H. K. Murthy, A. Melianas, Z. Tang, G. Juška, K. Arlauskas, F. Zhang, L. D. A. Siebbeles, O. Inganäs, and T. J. Savenije, Origin of reduced bimolecular recombination in blends of conjugated polymers and fullerenes, Adv. Funct. Mater. **23**, 4262 (2013).

[29] S. Shoaee, A. Armin, M. Stolterfoht, S. M. Hosseini, J. Kurpiers, and D. Neher, Decoding charge recombination through charge generation in organic solar cells, Sol. RRL **3**, 1900184 (2019).

[30] M. Azzouzi, N. P. Gallop, F. Eisner, J. Yan, X. Zheng, H. Cha, Q. He, Z. Fei, M. Heeney, A. A. Bakulin, and J. Nelson, Reconciling models of interfacial state kinetics and device performance in organic solar cells: Impact of the

energy offsets on the power conversion efficiency, Energy Environ. Sci. **15**, 1256 (2022).

[31] O. J. Sandberg and A. Armin, Energetics and kinetics requirements for organic solar cells to break the 20% power conversion efficiency barrier, J. Phys. Chem. C **125**, 15590 (2021).

[32] M. C. Heiber, C. Baumbach, V. Dyakonov, and C. Deibel, Encounter-limited charge-carrier recombination in phase-separated organic semiconductor blends, Phys. Rev. Lett. **114**, 136602 (2015).

[33] J. Benduhn, K. Tvingstedt, F. Piersimoni, S. Ullbrich, Y. Fan, M. Tropiano, K. A. McGarry, O. Zeika, M. K. Riede, C. J. Douglas, *et al.*, Intrinsic non-radiative voltage losses in fullerene-based organic solar cells, Nat. Energy **2**, 17053 (2017).

[34] M. Azzouzi, J. Yan, T. Kirchartz, K. Liu, J. Wang, H. Wu, and J. Nelson, Nonradiative energy losses in bulk-heterojunction organic photovoltaics, Phys. Rev. X **8**, 031055 (2018).

[35] X.-K. Chen, D. Qian, Y. Wang, T. Kirchartz, W. Tress, H. Yao, J. Yuan, M. Hülsbeck, M. Zhang, Y. Zou, *et al.*, A unified description of non-radiative voltage losses in organic solar cells, Nat. Energy **6**, 799 (2021).

[36] M. P. Langevin, Recombinaison et mobilités des ions dans les gaz, Ann. Chim. Phys. **28**, 433 (1903).

[37] O. J. Sandberg, M. Nyman, and R. Österbacka, Effect of contacts in organic bulk heterojunction solar cells, Phys. Rev. Appl. **1**, 024003 (2014).

[38] S. Selberherr, *Analysis and Simulation of Semiconductor Devices* (Springer-Verlag, Wien, 1984).

[39] D. L. Scharfetter and H. K. Gummel, Large-signal analysis of a silicon read diode oscillator, IEEE Trans. Electron Devices **16**, 64 (1969).

[40] H. K. Gummel, A self-consistent iterative scheme for one-dimensional steady state transistor calculations, IEEE Trans. Electron Devices **11**, 455 (1964).

[41] R. de Levie and H. Moreira, Transport of ions of one kind through thin membranes: I. General and equilibrium considerations, J. Membr. Biol. **9**, 241 (1972).

[42] For $x > x^*$, Eq. (4) is approximated as $\partial^2\phi(x)/\partial x^2 \approx qn_0(x)/\varepsilon\varepsilon_0$, where $n_0(x)$ is given by Eq. (14); in this region, we then find $\phi(x) = V_{\mathrm{BI},0} - V - (2kT/q)\ln((2kT/qF_0\lambda_{\mathrm{cat}})\sinh[(qF_0(d-x))/2kT + \sinh^{-1}(qF_0\lambda_{\mathrm{cat}}/2kT)])$, where $\lambda_{\mathrm{cat}} = \sqrt{2\varepsilon\varepsilon_0 kT/[q^2 n_{\mathrm{cat}}]}$. Equating this expression with Eq. (19) at $x = x^*$ in the case of Ohmic contacts ($\lambda_{\mathrm{an}}, \lambda_{\mathrm{cat}} \ll d$) yields $F_0(V) = \left[V_{\mathrm{BI},0} - V - (2kT/q)\ln\left(\left(q^2d^2\sqrt{p_{\mathrm{an}}n_{\mathrm{cat}}}\right)/2\varepsilon\varepsilon_0 kT\right) + (4kT/q)\ln(qF_0d/kT)\right]/d$ for small voltages. Applying Newton's iteration method once with $F_0 = (V_{\mathrm{BI}} - V)/d$ as the initial guess (where $V_{\mathrm{BI}} \equiv F_0(0)d$), $F_0(V)$ can be explicitly written as $F_0(V) \approx [V_{\mathrm{BI}} - V + (4kT/q)\ln(1-(V/V_{\mathrm{BI}}))(1-(4kT/(q[V_{\mathrm{BI}}-V])))^{-1}]/d$. Finally, we extend this expression beyond small V by using of a linear approximation of $F_0(V)$ between $V = 0$ and $V = V_{\mathrm{BI}}/2$ such that $F_0(V) \approx F_0(0) + [F_0(V_{\mathrm{BI}}/2) - F_0(0)](2V/V_{\mathrm{BI}})$, resulting in Eq. (21).

[43] A correction from diffusion is estimated as $\Delta J_{n,\mathrm{diff}} = \mu_n kT[\partial\Delta n/\partial x|_{x=d_{1/2}} - (\partial\Delta n/\partial x)|_{x=x_{Rn}}]$, where $d_{1/2} = (d + x_{Rn} - x_{Rp})/2$ is the midplane of the collection zone. Using Eq. (36), one finds $\Delta J_{n,\mathrm{diff}} = J^*_{\mathrm{gen}}(J^2kT/J^2_\beta qF_0d_{\mathrm{eff}})$. The corrected current density thus reads $J_{\mathrm{corr}} = J + \Delta J_{n,\mathrm{diff}}$, where J corresponds to the uncorrected current density. On the other hand, expanding the left-hand-side of Eq. (37), and solving for J yields $J = J^*_{\mathrm{gen}}/\sqrt{1+(J^*_{\mathrm{gen}}/J_\beta)^2}$. Hence, after combining everything together we find $J_{\mathrm{corr}} = J^*_{\mathrm{gen}}/\sqrt{1+(J^*_{\mathrm{gen}}/J_\beta)^2}\left[1 - (kT/qF_0d_{\mathrm{eff}})\left((J^*_{\mathrm{gen}}/J_\beta)^2/\sqrt{1+(J^*_{\mathrm{gen}}/J_\beta)^2}\right)\right]$. Finally, assuming the correction term to be much smaller than unity, we can approximate $J_{\mathrm{corr}} \approx J^*_{\mathrm{gen}}/\sqrt{1+(J^*_{\mathrm{gen}}/J_{\beta,\mathrm{corr}})^2}$, where $J_{\beta,\mathrm{corr}}$ is given by Eq. (38).

[44] L. J. A. Koster, M. Kemerink, M. M. Wienk, K. Maturová, and R. A. J. Janssen, Quantifying bimolecular recombination losses in organic bulk heterojunction solar cells, Adv. Mater. **23**, 1670 (2011).

[45] S. Zeiske, W. Li, P. Meredith, A. Armin, and O. J. Sandberg, Light intensity dependence of the photocurrent in organic photovoltaic devices, Cell Rep. Phys. Sci. **3**, 101096 (2022).

[46] A. M. Goodman and A. Rose, Double extraction of uniformly generated electron-hole pairs from insulators with noninjecting contacts, J. Appl. Phys. **42**, 2823 (1971).

[47] R. S. Crandall, Modeling of thin-film solar cells: Nonuniform field, J. Appl. Phys. **55**, 4418 (1984).

[48] V. D. Mihailetchi, J. Wildeman, and P. W. M. Blom, Space-charge limited photocurrent, Phys. Rev. Lett. **94**, 126602 (2005).

[49] Z.-E. Ooi, K. L. Chan, C. J. Lombardo, and A. Dodabalapur, Analysis of photocurrents in lateral-geometry organic bulk heterojunction devices, Appl. Phys. Lett. **101**, 053301 (2012).

[50] S. Wilken, O. J. Sandberg, D. Scheunemann, and R. Österbacka, Watching space charge build up in an organic solar cell, Sol. RRL **4**, 1900505 (2020).

[51] U. Rau, Reciprocity relation between photovoltaic quantum efficiency and electroluminescent emission of solar cells, Phys. Rev. B **76**, 085303 (2007).

[52] T. Kirchartz, J. Nelson, and U. Rau, Reciprocity between charge injection and extraction and its influence on the interpretation of electroluminescence spectra in organic solar cells, Phys. Rev. Appl. **5**, 054003 (2016).

[53] S. Schiefer, B. Zimmermann, and U. Würfel, Determination of the intrinsic and the injection dependent charge carrier density in organic solar cells using the suns-V_{OC} method, J. Appl. Phys. **115**, 044506 (2014).

[54] R. A. Street, A. Krakaris, and S. R. Cowan, Recombination through different types of localized states in organic solar cells, Adv. Funct. Mater. **22**, 4608 (2012).

[55] P. Hartnagel and T. Kirchartz, Understanding the light-intensity dependence of the short-circuit current of organic solar cells, Adv. Theory Simul. **3**, 2000116 (2020).

[56] D. Liraz, P. Cheng, Y. Yang, and N. Tessler, Light-induced trap emptying revealed by intensity-dependent quantum efficiency of organic solar cells, J. Appl. Phys. **131**, 135501 (2022).

[57] C. Wöpke, C. Göhler, M. Saladina, X. Du, L. Nian, C. Greve, C. Zhu, K. M. Yallum, Y. J. Hofstetter, D. Becker-Koch, *et al.*, Traps and transport resistance: the next frontier for stable state-of-the-art non-fullerene acceptor solar cells, Nat. Commun. **13**, 3786 (2022).

[58] O. J. Sandberg, S. Dahlström, M. Nyman, S. Wilken, D. Scheunemann, and R. Österbacka, Impact of a doping-induced space-charge region on the collection of photogenerated charge carriers in thin-film solar cells based on low-mobility semiconductors, Phys. Rev. Appl. **12**, 034008 (2019).

[59] J. Wu, J. Luke, H. K. H. Lee, P. Shakya Tuladhar, H. Cha, S.Y. Jang, W.C. Tsoi, M. Heeney, H. Kang, K. Lee, *et al.*, Tail state limited photocurrent collection of thick photoactive layers in organic solar cells, Nat. Commun. **10**, 5159 (2019).

[60] W. Tress, K. Leo, and M. Riede, Optimum mobility, contact properties, and open-circuit voltage of organic solar cells: A drift-diffusion simulation study, Phys. Rev. B **85**, 155201 (2012).

[61] O. J. Sandberg, A. Sundqvist, M. Nyman, and R. Österbacka, Relating charge transport, contact properties, and recombination to open-circuit voltage in sandwich-type thin-film solar cells, Phys. Rev. Appl. **5**, 044005 (2016).

[62] A. Spies, M. List, T. Sarkar, and U. Würfel, On the impact of contact selectivity and charge transport on the open-circuit voltage of organic solar cells, Adv. Energy Mater. **7**, 1601750 (2017).

[63] I. Zonno, B. Krogmeier, V. Katte, D. Lübke, A. Martinez-Otero, and T. Kirchartz, Discriminating between surface and bulk recombination in organic solar cells by studying the thickness dependence of the open-circuit voltage, Appl. Phys. Lett. **109**, 183301 (2016).

[64] A. Armin, A. Yazmaciyan, M. Hambsch, J. Li, P. L. Burn, and P. Meredith, Electro-optics of conventional and inverted thick junction organic solar cells, ACS Photonics **2**, 1745 (2015).

[65] L. Krückemeier, P. Kaienburg, J. Flohre, K. Bittkau, I. Zonno, B. Krogmeier, and T. Kirchartz, Developing design criteria for organic solar cells using well-absorbing non-fullerene acceptors, Commun. Phys. **1**, 27 (2018).

[66] J. G. Tait, U. W. Paetzold, D. Cheyns, M. Turbiez, P. Heremans, and B. P. Rand, Interfacial depletion regions: Beyond the space charge limit in thick bulk heterojunctions, ACS Appl. Mater. Interfaces **8**, 2211 (2016).

[67] M. Nyman, O. J. Sandberg, W. Li, S. Zeiske, R. Kerremans, P. Meredith, and A. Armin, Requirements for making thick junctions of organic solar cells based on nonfullerene acceptors, Sol. RRL **5**, 2100018 (2021).

[68] S. Zeiske, O. J. Sandberg, N. Zarrabi, W. Li, P. Meredith, and A. Armin, Direct observation of trap-assisted recombination in organic photovoltaic devices, Nat. Commun. **12**, 3603 (2021).

[69] W. Li, S. Zeiske, O. J. Sandberg, D. B. Riley, P. Meredith, and A. Armin, Organic solar cells with near-unity charge generation yield, Energy Environ. Sci. **14**, 6484 (2021).